THE ASTROPHYSICAL JOURNAL, 460:744–761, 1996 April 1

A NEAR-INFRARED STUDY OF THE K3-50 REGION OF HIGH-MASS STAR FORMATION

ERIC M. HOWARD,[1] JUDITH L. PIPHER,[1] WILLIAM J. FORREST,[1] AND C. G. DE PREE,[2,3]

Received 1995 May 18; accepted 1995 October 2

ABSTRACT

In an ongoing study of high-mass star formation regions in the near infrared (1–5 μm), we present J (1.2 μm), H (1.65 μm), K (2.23 μm), and L'' (3.81 μm) broadband images as well as Brγ ($n = 7 \rightarrow 4$, 2.166 μm) and Brα ($n = 5 \rightarrow 4$, 4.052 μm) hydrogen recombination line images, and 3.29 μm unidentified feature emission images of the K3-50 H II regions K3-50A and K3-50B, at a plate scale of $\sim 0\farcs33$ per pixel. The Brackett line images are combined with radio data to map the line-of-sight dust extinction to the compact H II region on small spatial scales. The 3.29 μm emission is found to overlap and extend beyond the Brα and Brγ emission into the photodissociation region. We find clumps of dust extinction that may indicate a cluster of stars is in the process of forming. The overall structure of region K3-50A appears to be that of a rotating torus of dense gas with a bipolar ionized gas outflow breaking through to the north and south.

Subject headings: dust, extinction — H II regions — infrared: ISM: continuum — infrared: ISM: lines and bands — ISM: individual (K3-50) — stars: formation

1. INTRODUCTION

K3-50 is a small, high-excitation optical nebula associated with a group of H II regions known collectively as W58. K3-50 is located approximately 8.7 kpc distant (Harris 1975), leading to a scale of $1'' = 0.04$ pc. In this paper we will concentrate primarily on the ultracompact H II region K3-50A and the more diffuse H II region K3-50B. K3-50A has a highly compact radio continuum shell structure with an $\sim 2''$ diameter, and a distinct break in the shell to the west (Turner & Matthews 1984). The radio peak is coincident with a strong 10 μm peak (Wynn-Williams et al. 1977), but displaced $\sim 2''$ northwest of the visual nebula. This displacement suggests that the source is partially obscured by a substantial dust cloud with the extinction varying strongly with position (Persson & Frogel 1974). The region is also the site of high-velocity CO emission that shows some evidence of originating in a bipolar outflow (Phillips et al. 1988; Phillips & Mampaso 1991), with the central core representing a region of significant kinematic activity within a very restricted ($\lesssim 1'$, 2.4 pc) area. De Pree et al. (1994) have imaged a bipolar outflow in the ionized gas at 2 cm.

The average extinction curve (τ_λ vs. λ) over the whole compact H II region K3-50A (from observations using apertures $\gtrsim 7''$) has been found to be substantially flatter than that for the average ISM (Natta & Panagia 1984). It has been postulated that the flatness is due to a strong variation of extinction with position across the region. By using high spatial resolution images of Brα and Brγ, we are able to provide information about the small-scale extinction to the region. The peak emission for K3-50A shifts with wavelength from radio to optical as a consequence of extinction gradients. High spatial resolution imaging at several near-infrared wavelengths is thus useful to study the spatial variation of the extinction, as well as to study the interaction of the embedded star(s) and/or young stellar object(s) (YSO) with the surrounding gas and dust.

Measurements of Brα and Brγ line flux images can yield an extinction estimate in two different ways. If a measurement of the optically thin radio flux density has been obtained for the same region, this radio flux density can be used to give a prediction of the intrinsic, unreddened Brα and Brγ line fluxes, for an assumed electron temperature and an assumed H^+-to-He^+ ratio. Comparing the observed Brackett measurement with the prediction gives an extinction measure. If, on the other hand, an extinction law is assumed, the Brα-to-Brγ ratio can be used to give a direct estimate of the extinction (Herter 1981; Herter et al. 1981). We have obtained Brα and Brγ images of K3-50A at high spatial resolution, along with broadband J (1.2 μm), H (1.65 μm), K(2.23 μm), and L'' (3.81 μm) images to study variations in the extinction to this region. Free-free radio continuum images at 14.7 GHz (first presented in De Pree et al. 1994) were also obtained.

Many H II regions exhibit emission at 3.29 μm that has been attributed to either polycyclic aromatic hydrocarbons (PAHs) or amorphous hydrocarbon solids. Precise identification of the emitting material has not been made. High spatial resolution images in the PAH feature can provide information on the environments where this material is found, and how well it survives under varying ultraviolet (UV) radiation fields. We have obtained images at 3.29 μm of K3-50A and K3-50B in an ongoing study of this feature emission.

2. OBSERVATIONS AND DATA REDUCTION

2.1. *Observations*

Initial observations were made with the University of Rochester's second-generation 58 × 62 InSb infrared array camera, mounted on the Mount Lemmon Observing Facility (MLOF) 60 inch (1.5 m) telescope in 1991 November. Higher signal-to-noise ratio observations were made with the University of Rochester's third-generation

[1] Department of Physics and Astronomy, University of Rochester, Rochester, NY 14627-0171.
[2] National Radio Astronomy Observatory, P.O. Box O, Socorro, NM 87801.
[3] Department of Physics and Astronomy, University of North Carolina at Chapel Hill, NC 27599-3255.

TABLE 1

FILTERS AND VALUES USED FOR CALIBRATIONS

Filter	λ_0 (μm)	$\Delta\lambda_{FWHM}$ (μm)	F_ν(0 mag) (Jy)
J	1.23	0.23	1685.5
H	1.65	0.32	1046.8
K	2.23	0.41	643.5
L''	3.81	0.63	248.0
Brα (1.73% CVF[a])	4.052	0.070	222.2
3.29 μm (2.07% CVF)	3.290	0.068	323.4
Brγ (2.39% CVF)	2.166	0.052	670.8

[a] Circular Variable Filter.

256 × 256 InSb infrared array camera at MLOF in 1994 February/March and at the Wyoming Infrared Observatory (WIRO) in 1994 July.

K3-50A [$\alpha(1950) = 19^h59^m50^s.1$, $\delta(1950) = 33°24'19''$] was imaged at J (1.2 μm), H (1.65 μm), and K (2.23 μm) on 1991 November 7, over a period of 20 minutes. Images at L'' (3.81 μm) were obtained on 1991 November 8, over a 10 minute period. Additional large mosaics of the K3-50 region were made at H and K in 1993 March at MLOF.

Brγ ($n = 7 \rightarrow 4$, 2.166 μm) and Brα ($n = 5 \rightarrow 4$, 4.052 μm) line and adjacent continuum observations were obtained on 1993 March 4, at MLOF. Additional Brα ($n = 5 \rightarrow 4$, 4.052 μm) line and adjacent continuum observations were obtained at the Wyoming Infrared Observatory (WIRO) on 1994 July 17, 20, and 21. The (MLOF) Brγ images were observed with 2.39% (equivalent width per wavelength) spectral resolution, while the (WIRO) Brα images were observed with 1.73% (equivalent width per wavelength) spectral resolution.

The 3.4 μm dust feature emission was searched for on 1993 March 5; however, this emission feature was not detected. Observations of the 3.29 μm dust feature were made on 1994 July 18 and 21 at WIRO with 2.07% spectral resolution (see Table 1). All observations were taken with interspersed off-source frames. These frames (background images) are used to subtract off atmospheric and instrumental background emission. Bias frames were taken by observing short integrations of a dark slide on the filter wheel for short integration times, in order to subtract off the electronic offset of the detector system before linearizing the 58 × 62 camera data. The bias subtraction step was not necessary with the 256 × 256 camera data because the bias was essentially zero for the Fowler sampling mode employed.

TABLE 2

PLATE SCALES

Observatory	Camera	Wavelength (μm)	Plate Scale (arcsec pixel^{-1})
MLOF.....	58 × 62	J (1.23)	0.90
MLOF.....	58 × 62	H (1.65)	0.93
MLOF.....	58 × 62	K (2.23)	0.89
MLOF.....	58 × 62	L'' (3.81)	0.91
MLOF.....	256 × 256	K (2.23)	0.326
MLOF.....	256 × 256	H (1.65)	0.326
MLOF.....	256 × 256	2.150	0.338
MLOF.....	256 × 256	4.052	0.336
WIRO	256 × 256	3.292	0.252
WIRO	256 × 256	4.052	0.251

2.2. *Data Reduction*

All images were linearized, background-subtracted and flat-fielded. The J, H, and K background frames include stars in the field. At each wavelength, individual frames were cross-correlated, shifted, corrected for optical distortion if necessary, and then co-added. Bad, noisy, and saturated pixels were flagged and not co-added into the final images.

Optical distortion of the 58 × 62 camera was measured by analyzing star pairs at K with known separations and position angles. A least-squares fitting routine was applied to determine the optic axis and distortion coefficient, as well as the plate scale (in arcseconds per pixel; see Table 2). Optical distortion of the 256 × 256 camera was measured by imaging graph paper in the lab. Then a least-squares fitting routine to an ideal grid was applied to determine the optic axis and distortion coefficient. The distortion was found to be negligible for WIRO observations, and no distortion correction was applied to those images.

The stars used for calibration, and their assumed magnitudes, are given in Table 3. A small air-mass correction was deduced using observations of standard stars at different air masses. This correction was then applied to each image.

The radio image obtained for use in combination with the infrared observations is a uniformly weighted, primary-beam response corrected, 14.7 GHz radio continuum image (originally presented by De Pree et al. 1994; see their paper for details on the radio observations and data reduction). The radio continuum image was reduced to match the plate scale of the infrared Brackett line images, and only the subsection of the radio continuum image that matched the

TABLE 3

STANDARD STARS

Standard Star	Wavelength	Assumed Magnitude	Date	Observatory
HD 203856.....	J	6.925	1991 Nov	MLOF
HD 203856.....	H	6.88	1991 Nov	MLOF
HD 203856.....	K	6.86	1991 Nov	MLOF
K3−50A 15''.....	L''	3.14	1991 Nov	MLOF
η Vir	2.166	3.765	1994 Feb	MLOF
ν Her.....	2.166	3.207	1994 Feb	MLOF
ν Her.....	4.052	3.154	1994 Mar	MLOF
HD 129655.....	K	6.69	1994 Mar	MLOF
HD 162208.....	H	7.145	1994 Mar	MLOF
γ Lyr	4.052	3.188	1994 Jul	WIRO
BS 8551.....	3.292	2.232	1994 Jul	WIRO
BS 8832.....	4.052	3.226	1994 Jul	WIRO
BS 8832.....	3.292	3.164	1994 Jul	WIRO

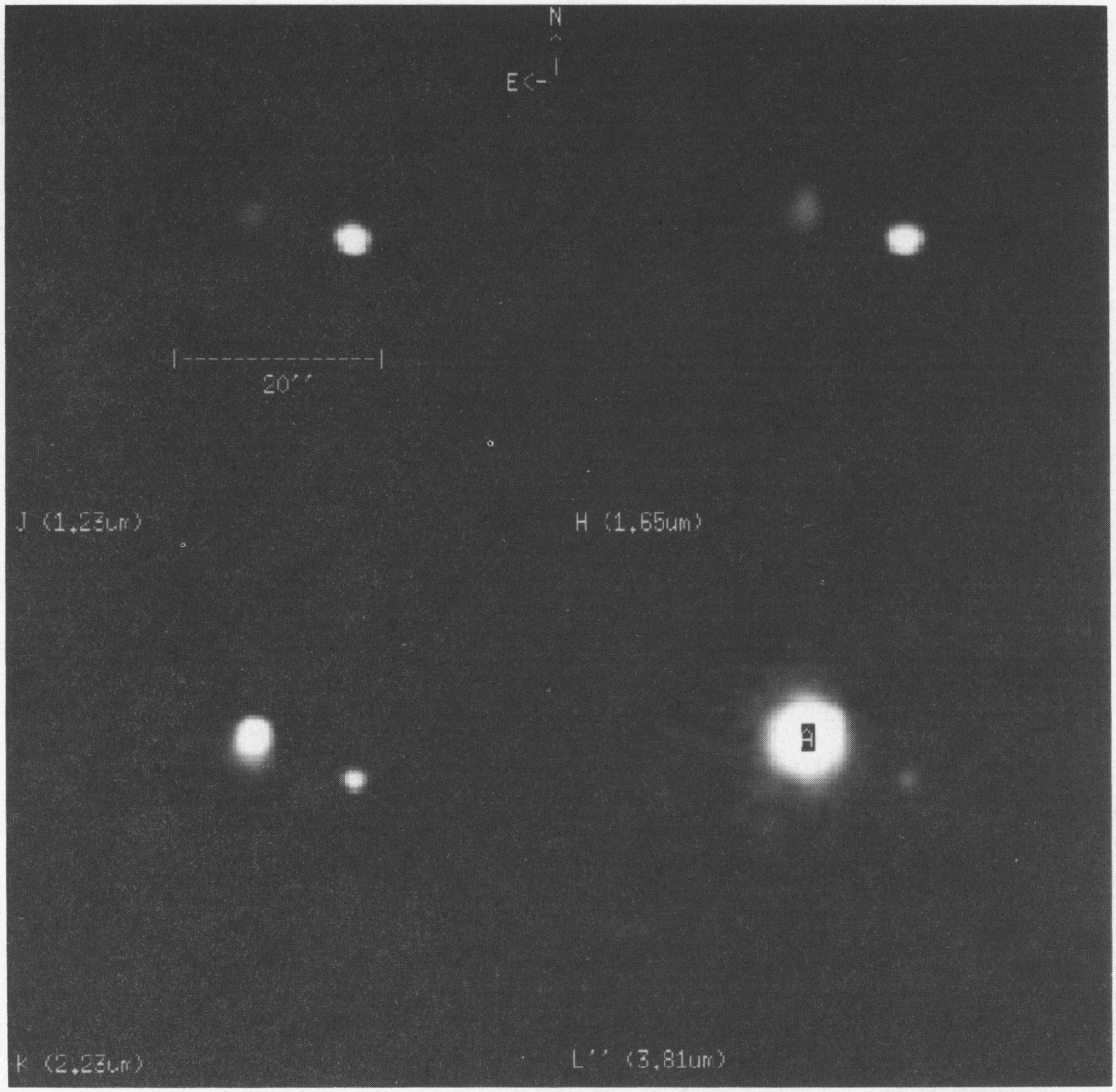

FIG. 1.—(*a*) K3-50A at *J* (1.23 μm). (*b*) K3-50A at *H* (1.65 μm). (*c*) K3-50A at *K* (2.23 μm). (*d*) K3-50A at *L*″ (3.81 μm). Object to the west of K3-50A is star 3 of Wynn-Williams (1977).

spatial extent of the Brackett line images was used. No correction was made to match spatial resolutions since the resolutions of the infrared data and the radio data were similar (∼1″.5 for the near-infrared [NIR] observations; 1″.4 × 1″.1 for the radio continuum observations). The radio continuum image was then used to generate an equivalent optically thin (EOT) radio continuum image by estimating the optical depth in the radio continuum from the radio continuum image itself.

2.3. *Image Results*

The data reduction process described above yielded the following images: small mosaics from 1991 November of K3-50A at *J*, *H*, *K*, and *L*″ are shown as Figures 1*a*, 1*b*, 1*c*, and 1*d*, respectively; Figure 2 (Plate 20) is a "true color" image of K3-50A, combining the *J*, *H*, and *K* images from Figure 1 together as blue, green, and red, respectively; large mosaics of the K3-50 region, including the H II regions K3-50A, K3-50B, K3-50C1, K3-50C2, and K3-50D (NGC 6857) at *H* and *K* are given as Figures 3 and 4, respectively; Brα and Brγ line flux images of the H II regions K3-50A and K3-50B are shown in Figures 5 and 6; Figure 7 shows the 3.29 μm dust feature emission in regions K3-50A and K3-50B. Since the seeing is variable, subtraction of continuum images from line + continuum images leads to residual structures near the locations of various point sources. The largest effect of this sort is seen in the Brγ image (Fig. 6) near the location of star 3 (see Fig. 4 for the position of star 3).

The final Brγ image is from the 1993 March observations. The final Brα image combines data from the 1993 March observations and the 1994 July observations to increase the signal-to-noise ratio. The final 3.29 μm image is from the 1994 July observations.

3. BRACKETT LINE IMAGES

3.1. *Morphology*

The morphology of the two Brackett line images is similar. Both show an unresolved (less than 2″) central source with a extension to the southeast and a dimmer extension to the northwest. The extension to the northwest is seen more clearly in the 14.7 GHz radio continuum image (Fig. 8 [Pl. 20]). There is extended Brγ emission in an arc from the southeast extension across to the southwest (see

PLATE 20

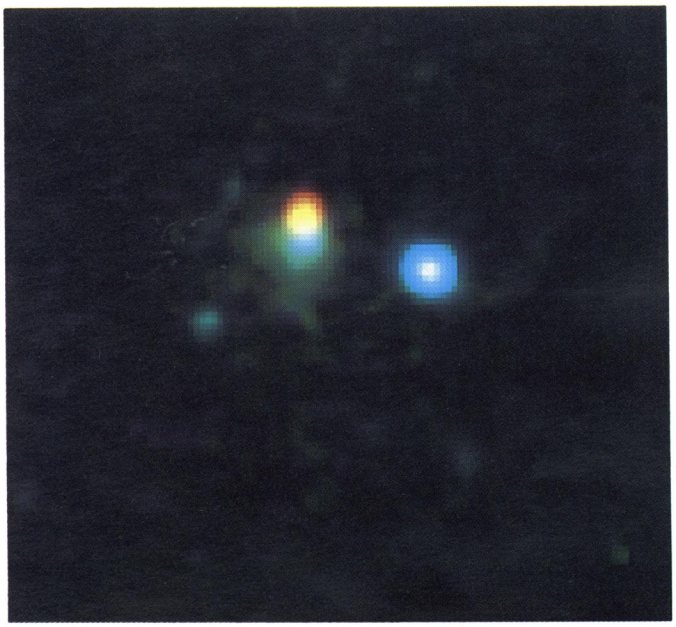

FIG. 2

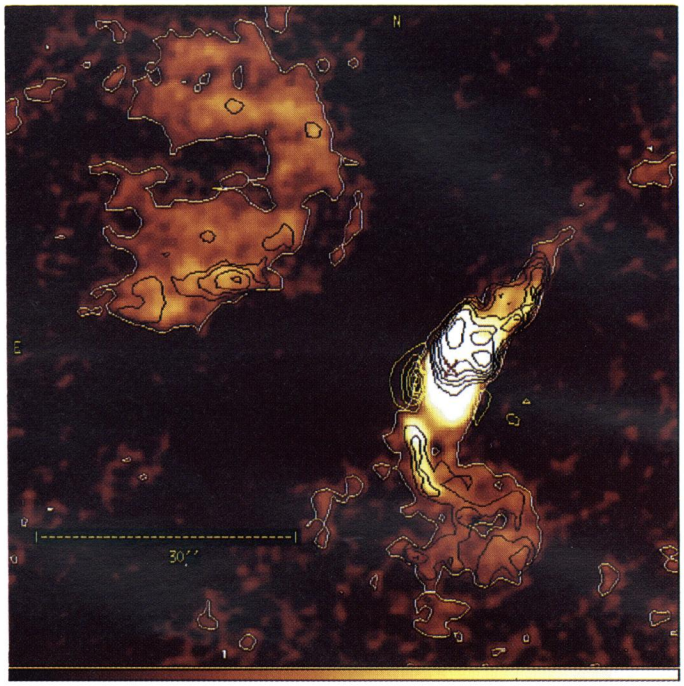

FIG. 8

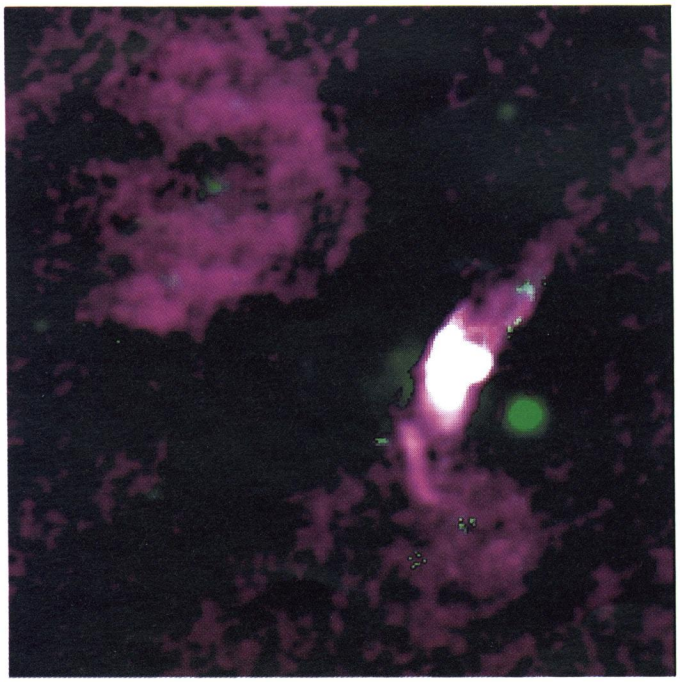

FIG. 13

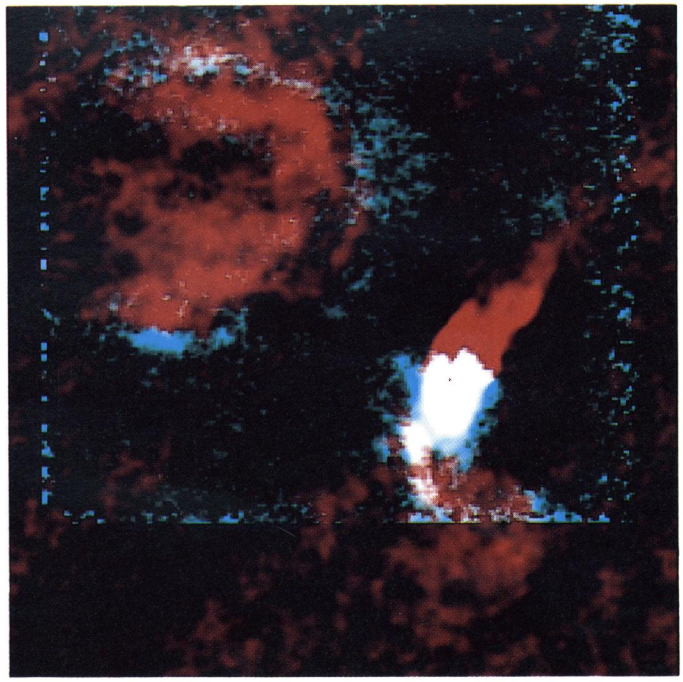

FIG. 17

FIG. 2.—"True color" image of K3 – 50A, J (1.23 μm), H (1.65 μm), and K (2.23 μm), are mapped to blue, green, and red, respectively. Object to the west is star 3 of Wynn-Williams (1977).

FIG. 8.—Equivalent optically thin 14.7 GHz radio continuum emission. White contours indicate 3 σ radio detection. Yellow contours trace regions of excess Brγ emission (i.e., scattered Brackett line emission; see § 3.1). Black contours trace dust extinction optical depth at 2.166 μm (see Fig. 9).

FIG. 13.—Composite, dereddened image at K (2.23 μm). The thermal gas component is displayed in purple; all other emission (scattered light, thermal dust emission, starlight) is displayed in green. Regions of overlap are indicated by white.

FIG. 17.—Emission at 3.29 μm (teal) overlaid on the radio continuum emission (red). Regions of overlap show as white.

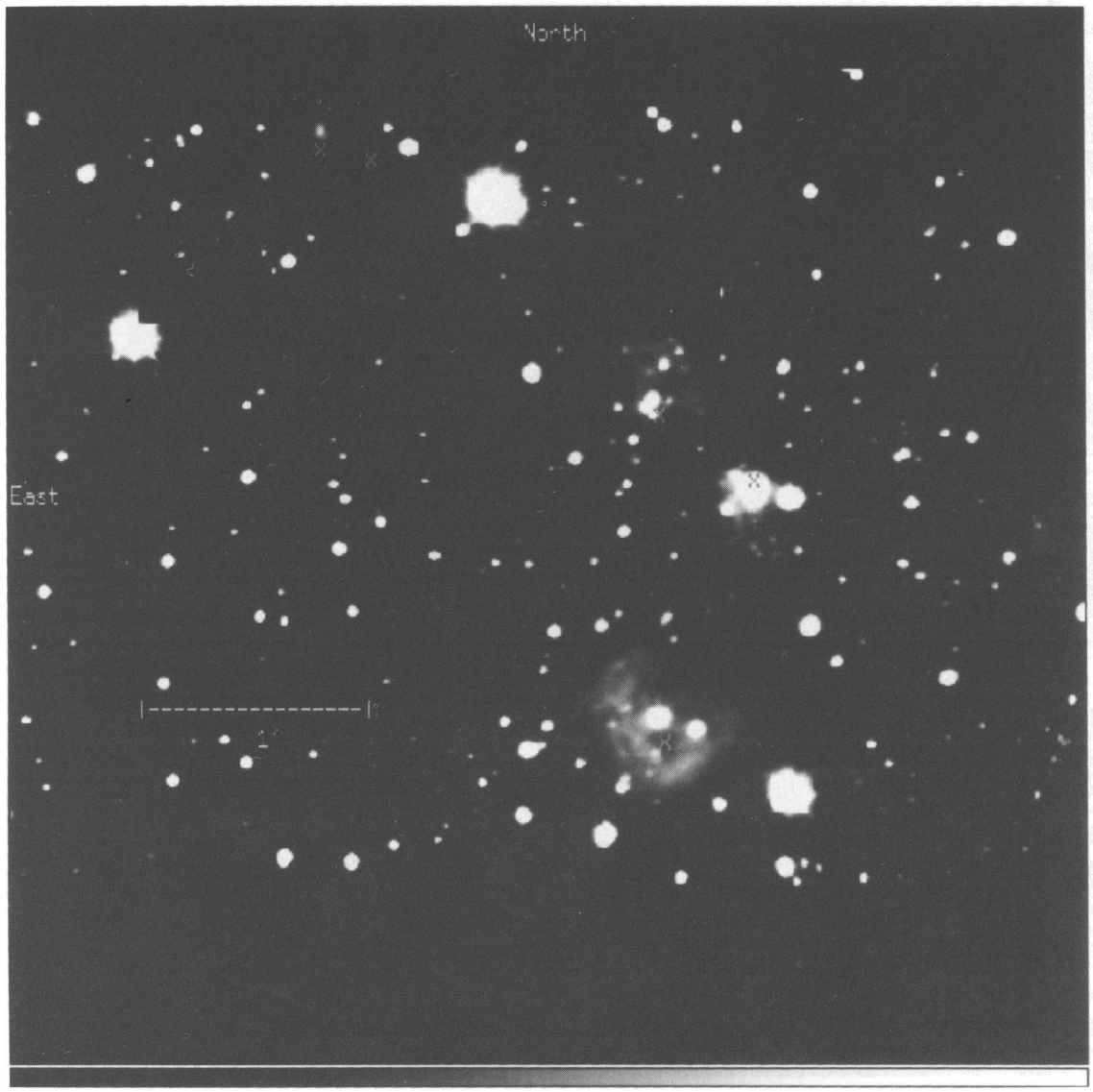

FIG. 3.—Mosaic of the K3-50 region at H (1.65 μm). Radio positions of De Pree et al. (1994) are marked with crosses (see Fig. 4).

Fig. 6). The overall shape is similar to an apostrophe. A similar structure is seen in Brα line emission, as well as in the radio emission.

The very high spatial resolution radio images of Turner & Matthews (1984) at 15 GHz show the central ultracompact H II region K3-50A is a shell (0.108 pc in diameter), with a break to the west and an extension to the southeast, along with an $\sim$0.″5 cavity. The authors claim the shell-to-cavity contrast ratio is too high to be consistent with a uniform shell.

Roelfsema, Goss, & Geballe (1988) observe roughly rectangular structures to the east and west of the peak emission in both the continuum and line images of Brα. We see no evidence of these structures in either of our Brackett line images or in the radio images, although the Brackett line emission does extend farther east-west than the radio emission (see below). We believe the reported structures are an artifact in Roelfsema et al.'s images. We do observe the extension to the southeast and the steeper emission gradient to the north relative to the extended radio emission; this indicates a region of high extinction north of K3-50A, even at 4 μm.

As previously noted, it appears that the Brackett line emission extends farther east-west than the radio emission near the radio peak. Specifically, there appears to be a region of Brackett line emission southeast of the radio peak, and another, dimmer region to the southwest, with no corresponding radio emission. Subtracting the Brackett line emission predicted from the radio emission (see § 3.2) from what is actually measured, we can estimate a lower bound to the amount of excess Brackett line emission. Any region that appears positive in such an image must have excess Brackett line emission, since extinction would generate negative features.

Since the radio image we are using has negative features because of incomplete u-v plane coverage (see DePree et al. 1994; namely, the trough between regions K3-50A and K3-50B) some of the "excess line emission" we estimate using the method above would be the result of these negative features. However, the excess is sufficiently high near region K3-50A (where the radio emission image is positive) that the excess appears to be real and not an artifact. In order to compensate for these negative radio features, we will first set all values less than zero to zero in the predicted

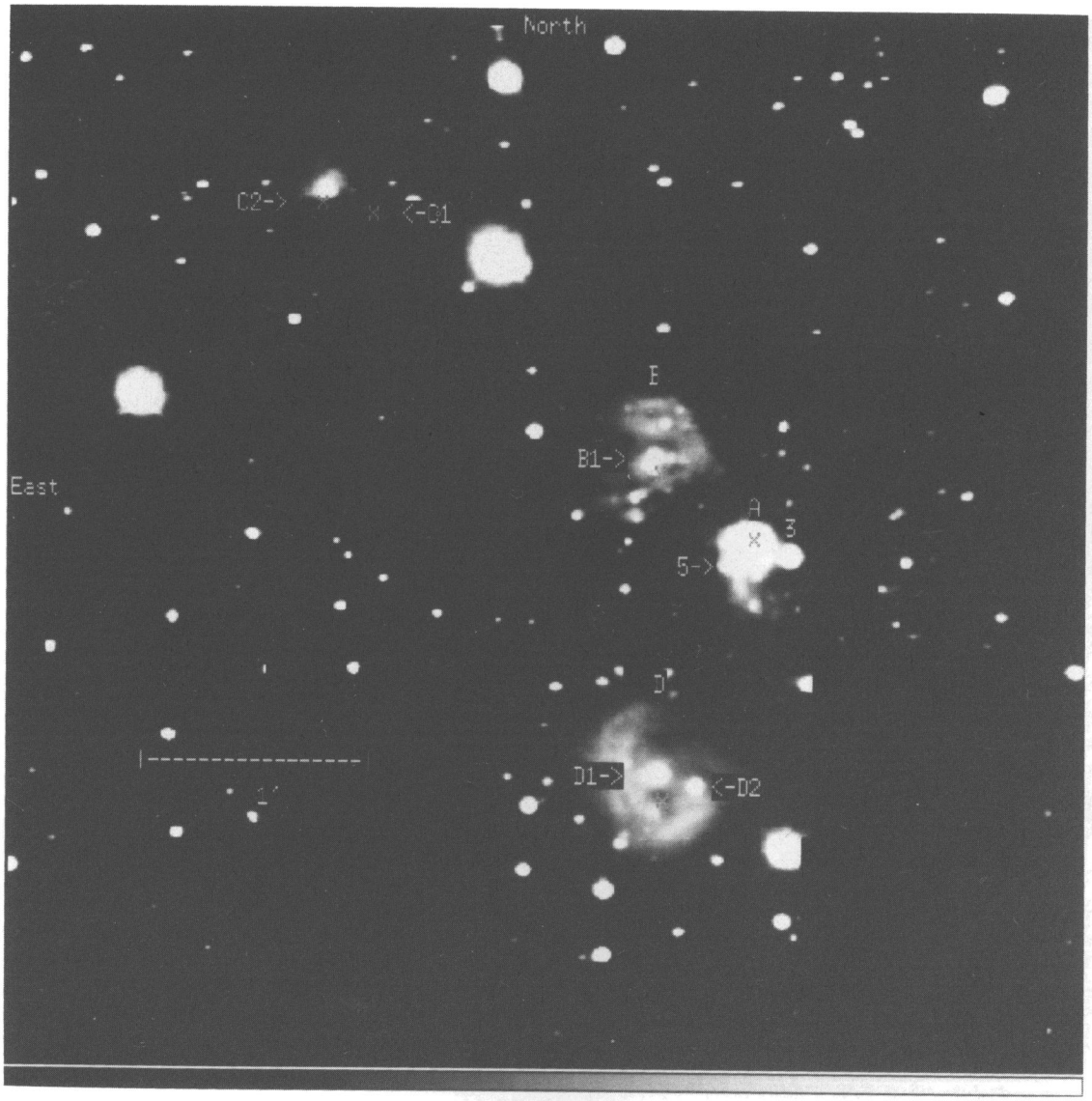

FIG. 4.—Mosaic of the K3-50 region at K (2.23 μm). Radio positions of De Pree et al. (1994) for H II regions A, B, C1, C2, and D are marked with crosses and labeled. The locations of stars B1, D1, D2, 3, and 5 are indicated (see § 4.1 and Table 4).

Brackett line images, before doing the subtraction. Figure 8 (EOT 14.7 GHz radio continuum emission) has contours of the "excess line emission" from Brγ (yellow) overlaid (see Fig. 8 legend for other contours). Our treatment, comparing the Brackett line emission with the radio emission in later sections, does not take this effect into account. Brγ photon scattering will lead to unrealistic (i.e., low to negative) estimates of extinction in the regions of the yellow contours in Figure 8, and will affect values in other regions if there is additional scattering of the Brackett line photons. Pure case B recombination line ratios may also be incorrect in these regions because of differential scattering of Brα against Brγ photons.

The emission measured in a 3".4 region centered in the brightest region of "excess line emission" is 2.6×10^{-13} ergs cm^{-2} s^{-1}. This is 7% of the value measured in a similar aperture located at the peak of the (reddened) Brγ emission.

3.2. *Comparison with Radio*

For a region with no extinction, the Brα and Brγ line fluxes are given by the following equations (Herter 1981; Herter et al. 1981):

$$F^{p}_{\mathrm{Br}\alpha} = 3.2 \times 10^{-11}\, S_{\nu}\,(\mathrm{Jy}) \left(\frac{\nu}{5\ \mathrm{GHz}}\right)^{0.1} \times \left(\frac{T_e}{7500\ \mathrm{K}}\right)^{-0.85} \mathrm{ergs\ cm^{-2}\ s^{-1}}, \quad (1)$$

$$F^{p}_{\mathrm{Br}\gamma} = 1.1 \times 10^{-11}\, S_{\nu}(\mathrm{Jy}) \left(\frac{\nu}{5\ \mathrm{GHz}}\right)^{0.1} \times \left(\frac{T_e}{7500\ \mathrm{K}}\right)^{-0.75} \mathrm{ergs\ cm^{-2}\ s^{-1}}, \quad (2)$$

where S_{ν} is the optically thin radio flux density in janskys (Jy) and T_e is the electron temperature. By comparing the predicted values of the Brα and Brγ fluxes with the observed values, one can determine the amount of extinction to the region from

$$F_{\lambda}^{\mathrm{observed}} = F_{\lambda}^{\mathrm{predicted}} e^{-\tau_{\lambda}}. \quad (3)$$

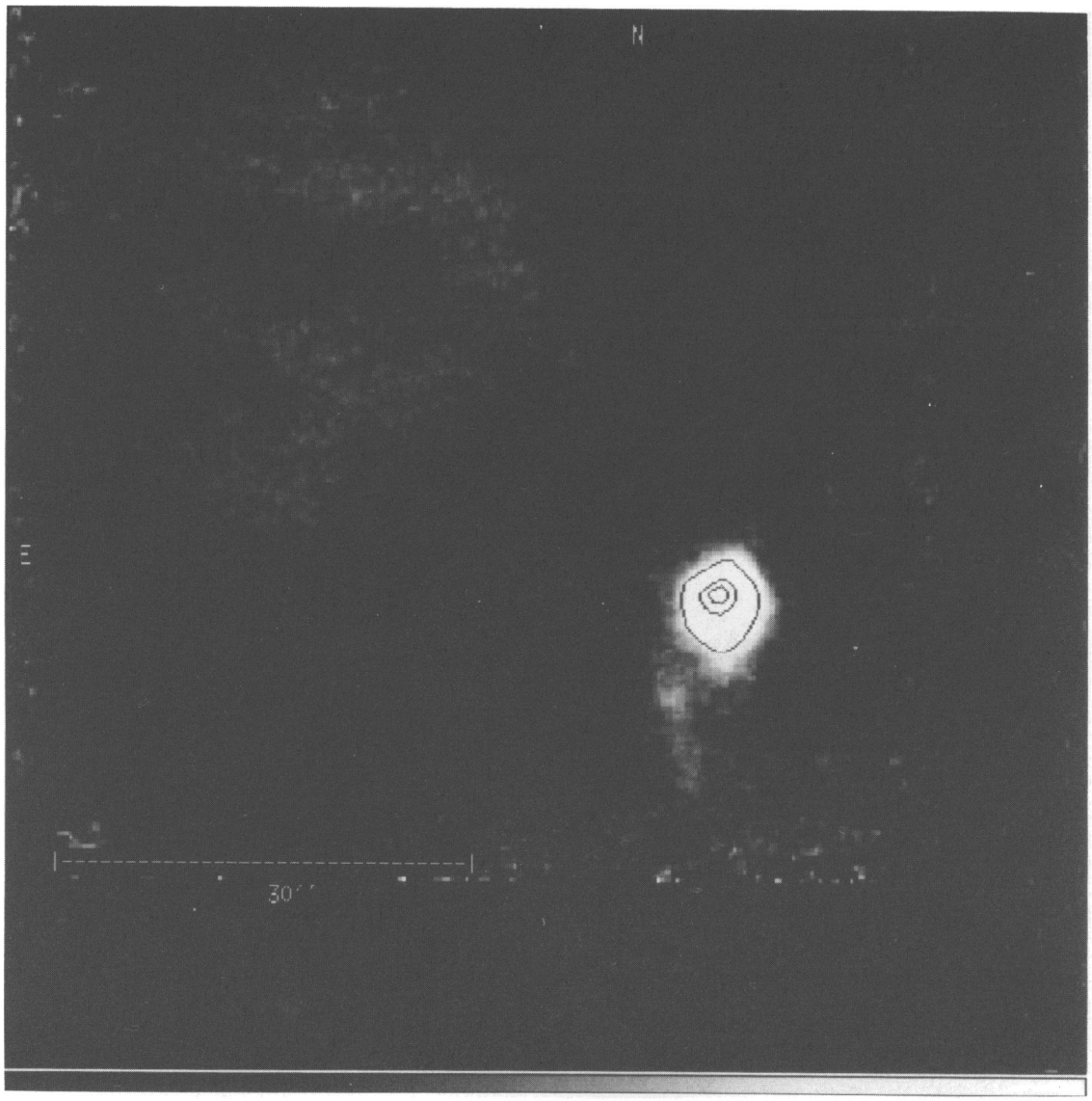

FIG. 5.—Brα ($n = 5 \rightarrow 4$, 4.052 μm) line minus continuum. Contours indicate the peak Brα emission.

These relations assume optically thin Brackett line and radio emission, a 10% abundance of He by number, and that all of the He is singly ionized. It is also assumed that none of the Brackett photons are scattered, as expected for most of the region, other than areas near the "excess line emission" region. The electron temperature (De Pree et al. 1994) determined from H76α measurements is 7900 ± 800 K for region K3-50A and 8100 ± 1900 K for region K3-50B. For simplicity, we shall adopt a value of 7500 K everywhere, when evaluating equations (1) and (2). A map of optically thin radio emission combined with maps of Brackett line emission thus provides a method of mapping the line-of-sight dust extinction optical depth in front of H II regions. We shall use this technique in the next section.

3.3. *Mapping Extinction: Method 1*

The measured radio brightness temperature (T_b) in the 14.7 GHz image is given by

$$T_b = T_e(1 - e^{-\tau_\nu}) . \quad (4)$$

If the emission were optically thin, it would be given by

$$T'_b = T_e \tau_\nu , \quad (5)$$

so that the corrected optically thin emission is given by

$$T'_b = \frac{T_b \tau_\nu}{1 - e^{-\tau_\nu}} . \quad (6)$$

If the electron temperature is measured, equation (4) can be solved for the τ_ν image, and that can be used with equation (5) to generate the EOT image. The correction for optical depth in the radio image at the peak pixel in region K3-50A was 41%; however, the correction over most of regions K3-50A and K3-50B was less than 0.03%. Using the EOT 14.7 GHz radio image, we generated images of the line-of-sight dust extinction optical depth at 4.052 and 2.166 μm. excluding scattered Brackett line photons, using equations (1) and (2) in combination with equation (3). The uncertainty in both the radio continuum flux density (see De Pree et al. 1994) and the Brγ line emission flux is 20%, giving an uncertainty in the dust extinction of ~28% or ~0.3 in optical depth at 2.17 μm. This degree of uncertainty does not affect our conclusions. This process generated Figures 9 and 10 (dust extinction optical depth maps at 2.166 and 4.052 μm, respectively). The dust extinction across region

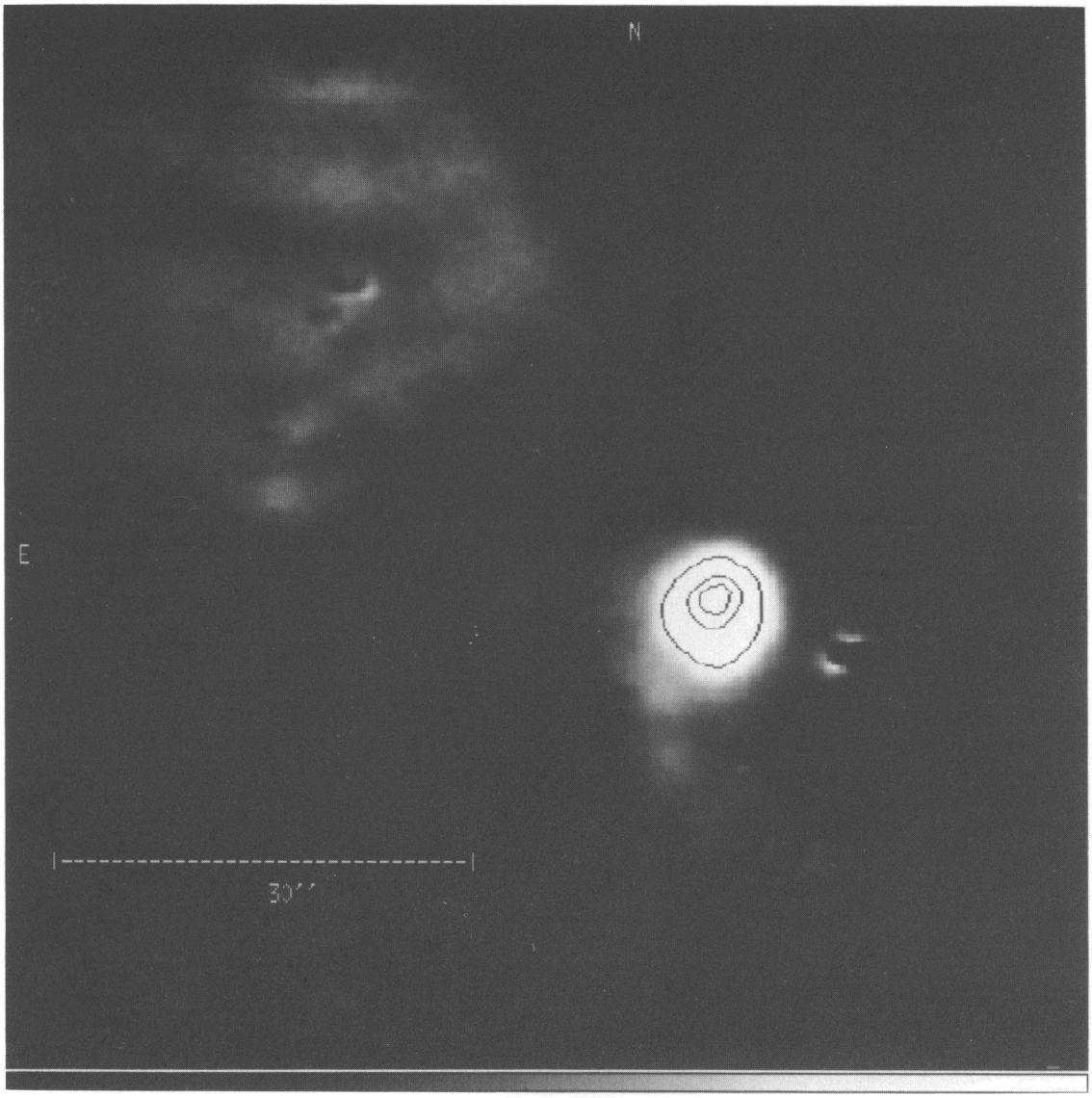

FIG. 6.—Brγ ($n = 7 \rightarrow 4$, 2.166 μm) line minus continuum. Contours indicate the peak Brγ emission. Because of seeing variations, some of the point sources did not subtract well.

K3-50A at 4.052 μm ($\tau_{4.05}$) varies from 0 to 3 in regions of high signal-to-noise ratio, with an average value in the central 2".7 of $\sim$0.6. At 2.166 μm the dust extinction optical depth ($\tau_{2.17}$) varies from 0 to 4 with an average value in the central 2".7 of $\sim$2.0. However, the extinction varies dramatically across the source. The average $\tau_{2.17}$ to the south of K3-50A is $\sim$0.6, while to the north it is $\sim$3.3. This indicates that the average visual extinction (A_v) varies from 6 to greater than 30 mag within 10" of the radio peak.

The value of the dust extinction optical depth to the larger, more diffuse H II region K3-50B, determined by this method, is a lower bound because of "missing" flux density in the interferometric radio data, since there is a lack of sensitivity to large-scale structures. For this reason we have set $\tau_{2.17}$ in region K3-50B to zero in Figures 9 and 10. We will address the absolute value of the extinction to region K3-50B using the Brα and Brγ data with an assumed dust extinction power law, to generate an alternative extinction optical depth map (see § 3.4).

If we assume a power-law dependence of extinction on wavelength (see § 3.4), $\tau_\lambda \propto \lambda^{-\alpha}$, the images of $\tau_{4.05}$ and $\tau_{2.17}$ can be used to map the power-law exponent, α (Fig. 11). We find an average value of $\alpha = 1.5$ in the central 2".7, flatter than that for the general ISM ($\alpha_{ISM} \simeq 1.8$; Martin & Whittet 1990; van de Hulst 1946), but consistent with previous measurements of α in the high-mass star formation region Mon R2 (Howard, Pipher, & Forrest 1994; $\alpha = 1.4$). The extinction power law clearly varies across K3-50A. Looking at only the region with the highest signal-to-noise ratio, α varies from values near 1 to the south of the radio point-source center to a peak of 2.4 near the center of region K3-50A to values around 0.4 to the north (where the dust extinction is highest).

The infrared extinction law above assumes that the extinction is foreground and that any light scattered in the cloud is lost to the observer and thus adds to the extinction. Much of the extinction in K3−50 is caused by local clouds of dust. In this case, light will be scattered both into and out of the line of sight. The absorptive fraction of the extinction will be unaffected, but the scattering fraction will be effectively reduced as compared with the assumption of foreground dust extinction. Since scattering is more effective at

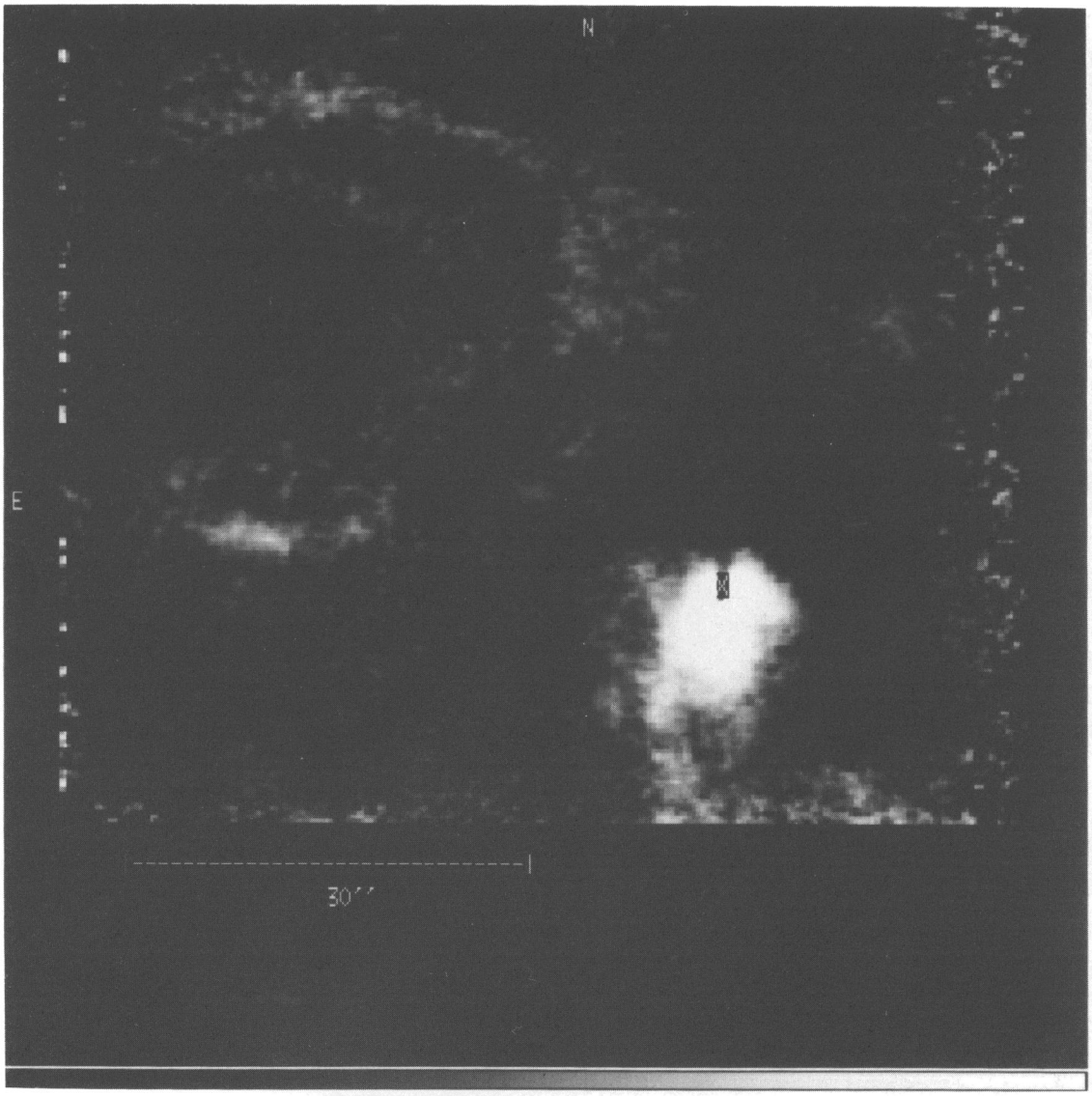

FIG. 7.—Emission at 3.29 μm. The continuum has been subtracted. The radio peak is indicated with a cross. Note the double-shell structure in region B, to the northeast.

shorter wavelengths, this process should also generate a flatter extinction curve than that observed for the general ISM.

Natta & Panagia (1984) propose that variations in the extinction on scales smaller than our resolution, caused by clumps of denser material, can lead to a flattening of the observed extinction curve. The grain properties of the material causing the extinction may thus be the same as those in the general interstellar medium and have an extinction-law index of $\alpha \sim 1.8$, while the clumpiness of the material gives rise to the lower observed values.

Alternatively, the grains surrounding the K3-50A region may be modified by the interaction of the dense environment and stars present. Larger grains, such as those with highly porous ice mantles or coagulations of smaller grains, can lead to a flattening of the extinction law (Draine & Lee 1984).

3.4. *Mapping Extinction: Method 2*

If the wavelength dependence of extinction is assumed to be a power-law, as given above, the ratio of $F^{ob}_{Br\alpha}/F^{ob}_{Br\gamma}$ can give a measure of the differential dust extinction optical depth, as follows from equation (3),

$$\frac{F^{ob}_{Br\alpha}}{F^{ob}_{Br\gamma}} = \frac{F^{p}_{Br\alpha}}{F^{p}_{Br\gamma}} e^{\tau_{Br\gamma} - \tau_{Br\alpha}}, \quad (7)$$

where F^p_λ is given by equations (1) and (2) and the ratio $F^p_{Br\alpha}/F^p_{Br\gamma}$ reduces to 3.2/1.1 for $T_e = 7500$ K. The equation

$$\frac{\tau_{2.17}}{\tau_{4.05}} = \left(\frac{2.166}{4.052}\right)^{-\alpha} \quad (8)$$

then gives the relation needed to generate the individual optical depth estimates. However, it is still necessary to assume a value of α. If we assume $\alpha = 1.5$, the measured average across K3-50A determined by method 1, we then generate Figure 12. The average value of $\tau_{2.17}$ across region K3-50B using this second method is ~ 1.15, which gives an A_v of ~ 12 mag. If we instead assume a value of $\alpha = 1.8$ as is found for the general ISM (Martin & Whittet 1990), we find an average value of $\tau_{2.17} \sim 1.04$ or $A_v \sim 11$ mag across K3-50B. The extinction map generated by this second method is very similar to that generated by the first method across region A, except in regions north of the radio contin-

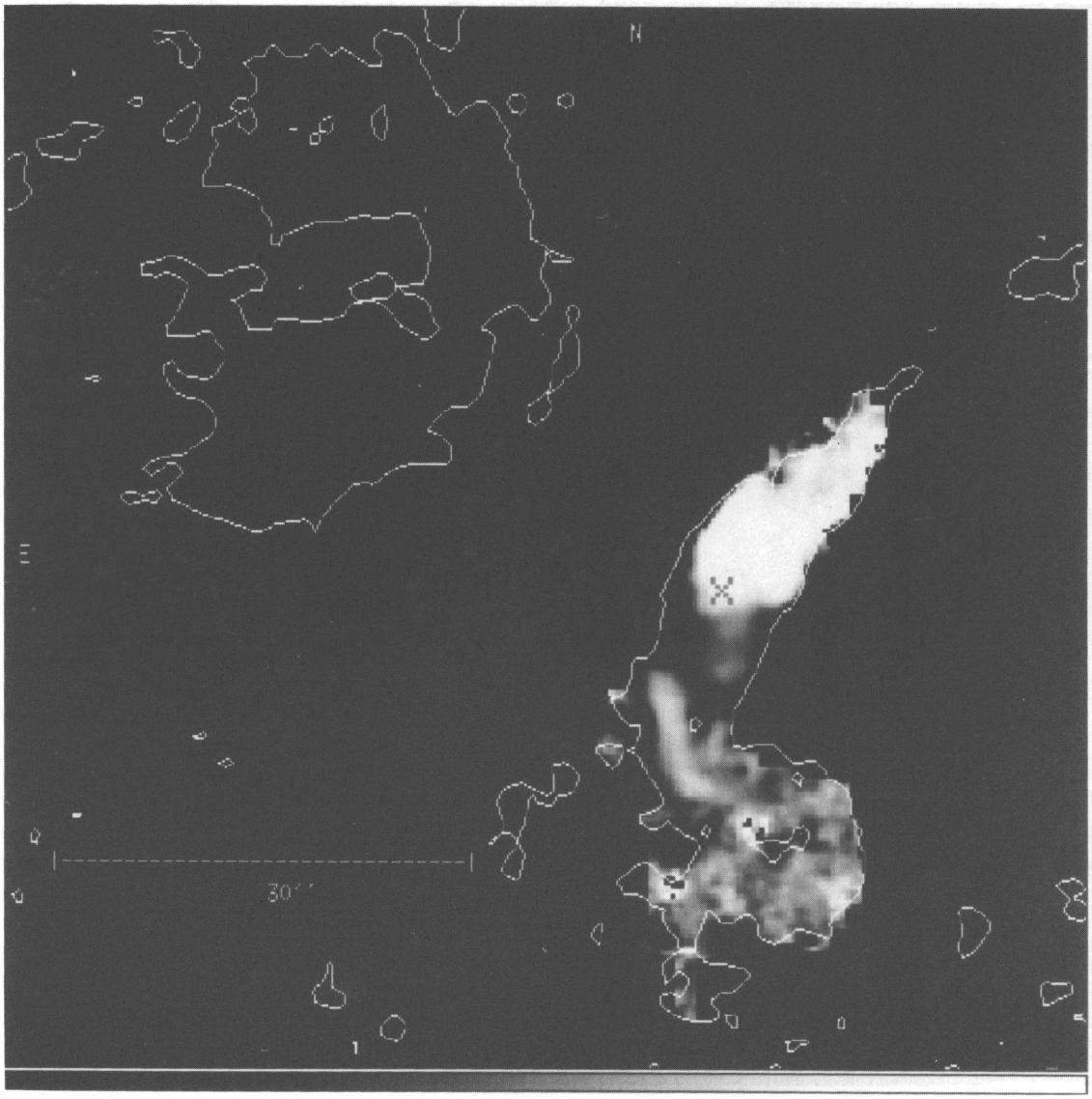

FIG. 9.—Dust extinction optical depth at 2.166 μm generated from a ratio of the radio continuum image and the Brγ image. The image is scaled from 0 (*black*) to 4 (*white*) on a square root scale and is overlaid with 3 σ contours from the 14.7 GHz image. The radio peak is marked with a cross. Region B has been set to zero (see text).

uum peak. In this region the dust is dense enough to cause substantial extinction of the Brα line emission, resulting in an underestimate of the extinction in this region (as is clearly seen in a comparison of Figs. 10 and 12). We estimate an error of 28% ($\sim$0.3 in optical depth at 2.17 μm) in the extinction maps, which does not alter our conclusions.

3.5. *Discussion of Extinction Morphology: A Stellar Cluster in the Process of Forming?*

The dust extinction optical depth is largest north and overlapping the peak of emission in region K3-50A (Fig. 9). There is a clear hole in the extinction to the south–east and a region of lower extinction to the south of the peak. This is the location of the optical nebulosity (see Fig. 2). Further south, along the tail of ionized gas emission, the extinction increases again to a value consistent with the value of extinction over most of region K3-50B.

In the region of highest extinction, north of the radio peak, there are two clumps of high extinction, $\sim$3″ in size. The dereddened Brγ flux (see § 4.1) from clump 1 (to the northwest; see Fig. 9) in a 3″ aperture is 3.8×10^{-12} ergs cm^{-2} s^{-1}; for clump 2 (directly north of the radio peak), which coincides with the peak ^{13}CO emission of Sargent et al. (1985), we measure a flux of 9.7×10^{-12} ergs cm^{-2} s^{-1}. The flux near the radio peak is 3.2×10^{-11} ergs cm^{-2} s^{-1}. If these Brackett line measurements are used to estimate the number of Lyman continuum photons (see eq. [1], and see Turner & Matthews 1984) from each clump, and if we then use Panagia (1973) to estimate the stellar-type from the number of Lyman continuum photons, we find that clump 1 could be powered by an O9.5 star, clump 2 by an O8.5 star, and the region near the radio peak by an O6.5 star. This would leave $\sim$2.1 Jy of excess radio flux density from region K3-50A, sufficient to be the emission of one or more O-type stars or a number of B-type stars. Alternatively, a single O4 or O5 star may be the source of all of the emission.

Region K3-50B has a clumpy extinction structure that uniformly covers the area except for the southwestern corner of the H II region. Here the extinction is higher again and probably connects with the high-extinction region to the north of K3-50A.

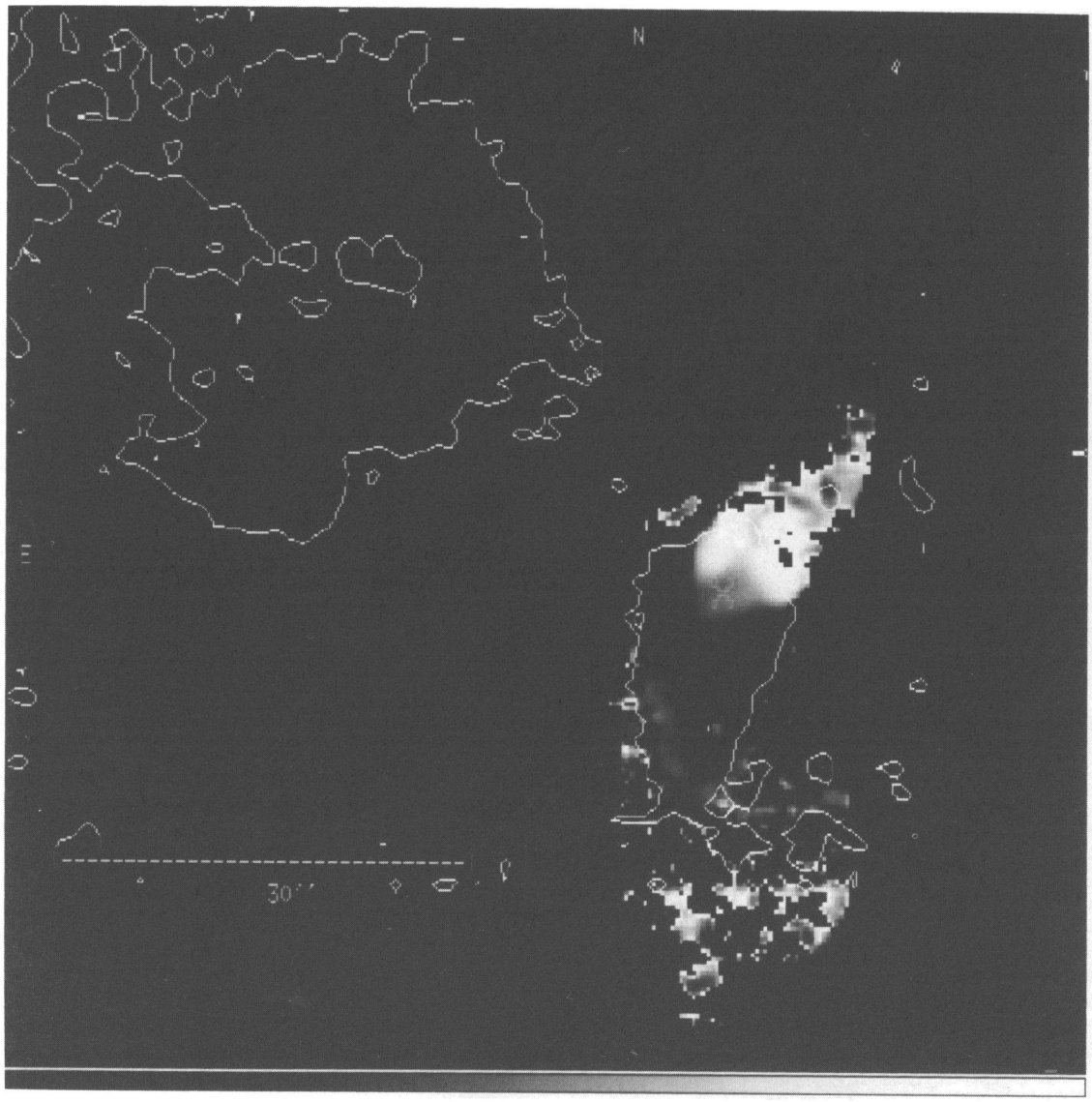

FIG. 10.—Dust extinction optical depth at 4.052 μm generated from a ratio of the radio continuum image and the Brα image. The image is scaled from 0 (*black*) to 4 (*white*) on a square root scale and is overlaid with 3 σ contours from the Brα image. The radio peak is marked with a cross. Region B has been set to zero (see text).

The average visual extinction to region K3-50C1 is ~92 mag (Roelfsema et al. 1988), and there is no clear extended emission visible in our broadband images (see Figs. 3 and 4), though there are dim point sources that may be related to the H II region. The average visual extinction to region K3-50C2 is ~32 mag (Roelfsema et al. 1988), and its radio emission peak is obscured in our broadband images. However, the extended emission to the north of K3-50C2 is clearly associated with this H II region and is brighter at *H* and much brighter at *K* than the radio peak position to the immediate south, indicating a gradient in extinction across this source. De Pree Mehringer & Goss (1996) have imaged region K3-50C1 in H92α, and it appears to be an outflow source of ionized gas.

Region K3-50D, to the south of K3-50A, lies behind only ~2 mag of visual extinction (Roelfsema et al. 1988) and is clearly visible in optical photographs of the region (Wynn-Williams et al. 1977).

The overall picture is thus one of increasing extinction as the region is viewed from south to north, but it is not a smooth increase. There are holes (south of region K3-50A) and dust lanes (one across K3-50C1 and K3-50C2 and another from the south edge of K3-50B, continuing west along the north edge of K3-50A). There is clearly structure in the dust extinction down to the 1.″5 level (0.06 pc).

3.6. *Comparison With Other Hydrogen Line Measurements*

As a check on our absolute calibrations, we shall now compare our Brackett line observations with previous measurements in the literature. Roelfsema et al. (1988) quote $6.8 \pm 0.3 \times 10^{-11}$ ergs cm^{-2} s^{-1} line flux at Brα in a 25″ aperture centered on the peak emission. Our measurement in a 25″ software aperture is $8.1 \pm 1.6 \times 10^{-11}$ ergs cm^{-2} cm^{-2} s^{-1}. Thompson & Tokunaga (1980) quote a value of $5.2 \pm 0.3 \times 10^{-12}$ ergs cm^{-2} s^{-1} for the Brγ line flux in a 7″ aperture. Our 7″ software aperture measurement is $7.2 \pm 1.4 \times 10^{-12}$ ergs cm^{-2} s^{-1}. Both of our measurements are thus somewhat higher than previous measurements. The Brα measurement is within 20% of the previous measurement, consistent with the uncertainties in calibration and continuum subtraction. The Brγ value has a higher deviation (30%) from the value in the literature;

PLATE 20

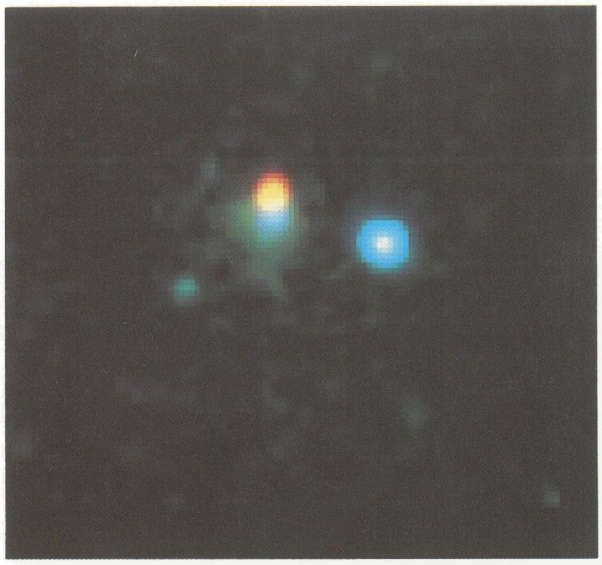

FIG. 2

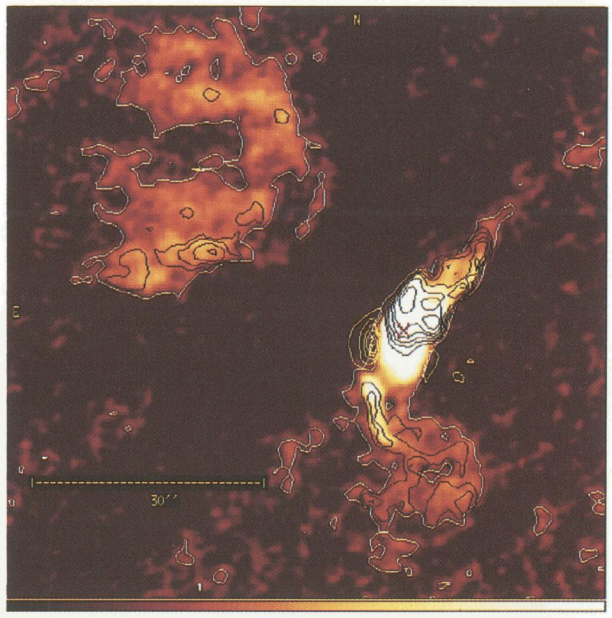

FIG. 8

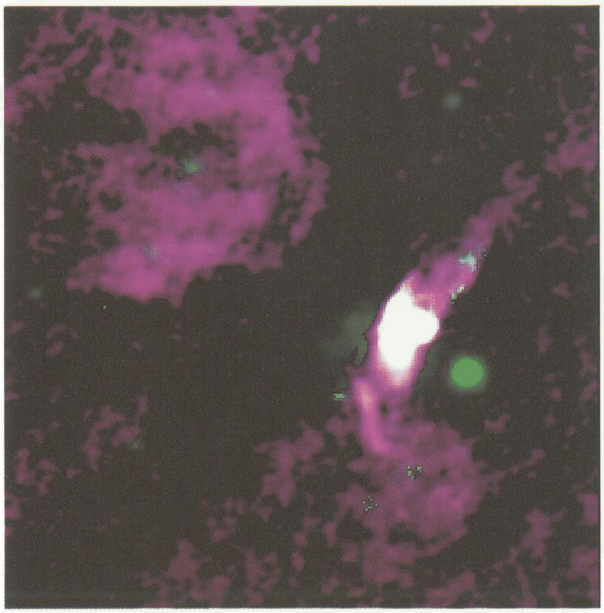

FIG. 13

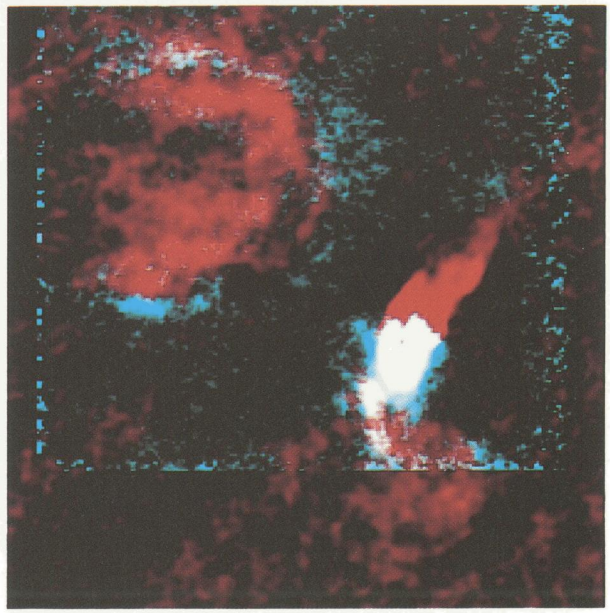

FIG. 17

FIG. 2.—"True color" image of K3 – 50A, J (1.23 μm), H (1.65 μm), and K (2.23 μm), are mapped to blue, green, and red, respectively. Object to the west is star 3 of Wynn-Williams (1977).

FIG. 8.—Equivalent optically thin 14.7 GHz radio continuum emission. White contours indicate 3 σ radio detection. Yellow contours trace regions of excess Brγ emission (i.e., scattered Brackett line emission; see § 3.1). Black contours trace dust extinction optical depth at 2.166 μm (see Fig. 9).

FIG. 13.—Composite, dereddened image at K (2.23 μm). The thermal gas component is displayed in purple; all other emission (scattered light, thermal dust emission, starlight) is displayed in green. Regions of overlap are indicated by white.

FIG. 17.—Emission at 3.29 μm (teal) overlaid on the radio continuum emission (red). Regions of overlap show as white.

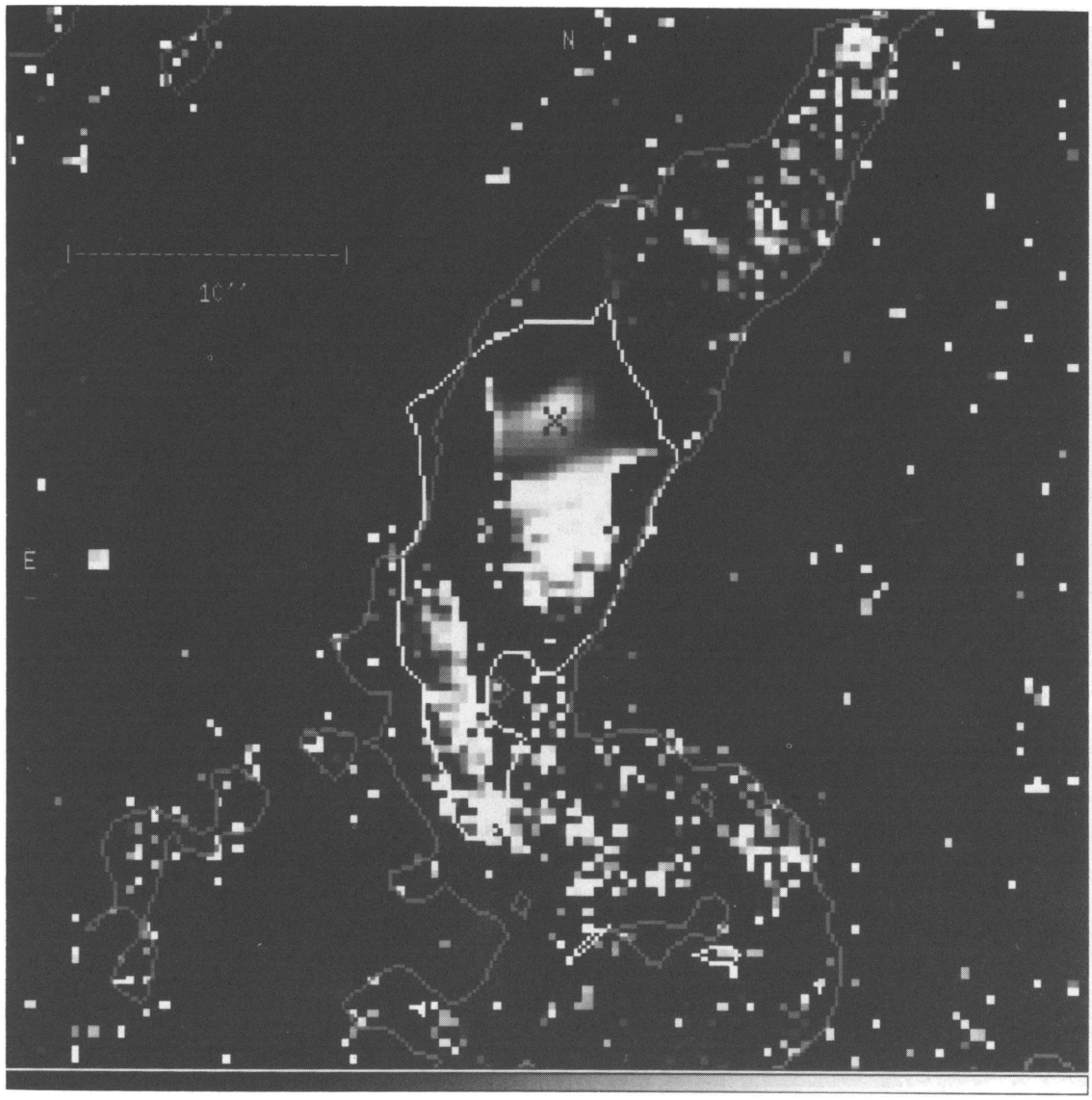

FIG. 11.—Map of the dust extinction power-law exponent α ($\tau_\lambda \propto \lambda^{-\alpha}$) over H II region *A*, scaled from 0 (*black*) to 3 (*white*). Image is overlaid with 3 σ contours from the Brα image. The radio peak is marked with a cross.

however, a small change in the central position of our synthetic aperture (less than 1″) reproduces values consistent with the literature, indicating that uncertainties in alignment of the apertures may be the source of the discrepancy.

4. BROADBAND IMAGES

4.1. *Dereddening*

We can use the image of the line-of-sight extinction to the H II region, $\tau_{2.17}$, to generate extinction images at other wavelengths, for regions of overlap with the Brackett line images, assuming that the extinction is external to the emitting region.

Figures 13–16 (Plate 20) are dereddened images at *K* and *H*. The images use the dust extinction optical depth image (Fig. 9) in combination with the extinction law ($\tau_\lambda \propto \lambda^{-1.5}$) to correct the overlap region and sets the dust extinction optical depth to zero outside this region (see Fig. legend).

4.2. *Region K3-50A*

There is a shift in the position of the peak emission as we change wavelengths from 3.8 to 1.2 μm (see Figs. 1*a*–1*d* and 2). The *L*″ image is uniform, indicating that the extinction is not enough to alter the morphology substantially at this wavelength, and we are seeing primarily a point source with size $\lesssim$2″.3 FWHM. The spatial extent of the emission at *L*″ indicates that the source of this emission is less than or equal in size to the ultracompact H II radio shell seen by Turner & Matthews (1984). The emission at *L*″ is predominantly hot dust grain emission.

The morphology of the emission at *K* is quite different. The peak of the emission is shifted slightly south, and extended emission is seen to the east and south. In the *K*-band we are seeing emission from the central object, starlight, thermal gas emission, transiently heated grain emission, and scattered light. We estimate the thermal gas emission (TGE; includes free-free, free-bound, line radiation, and two-photon emission) to the *K* and *H* bands from

$$F_H^{\rm TGE}\ ({\rm Jy}) = 0.24 S_{5\ {\rm GHz}}\ , \tag{9}$$

$$F_K^{\rm TGE}\ ({\rm Jy}) = 0.26 S_{5\ {\rm GHz}} \tag{10}$$

(Woodward 1987), assuming optically thin emission and no extinction. We find that the extended nebulosity from

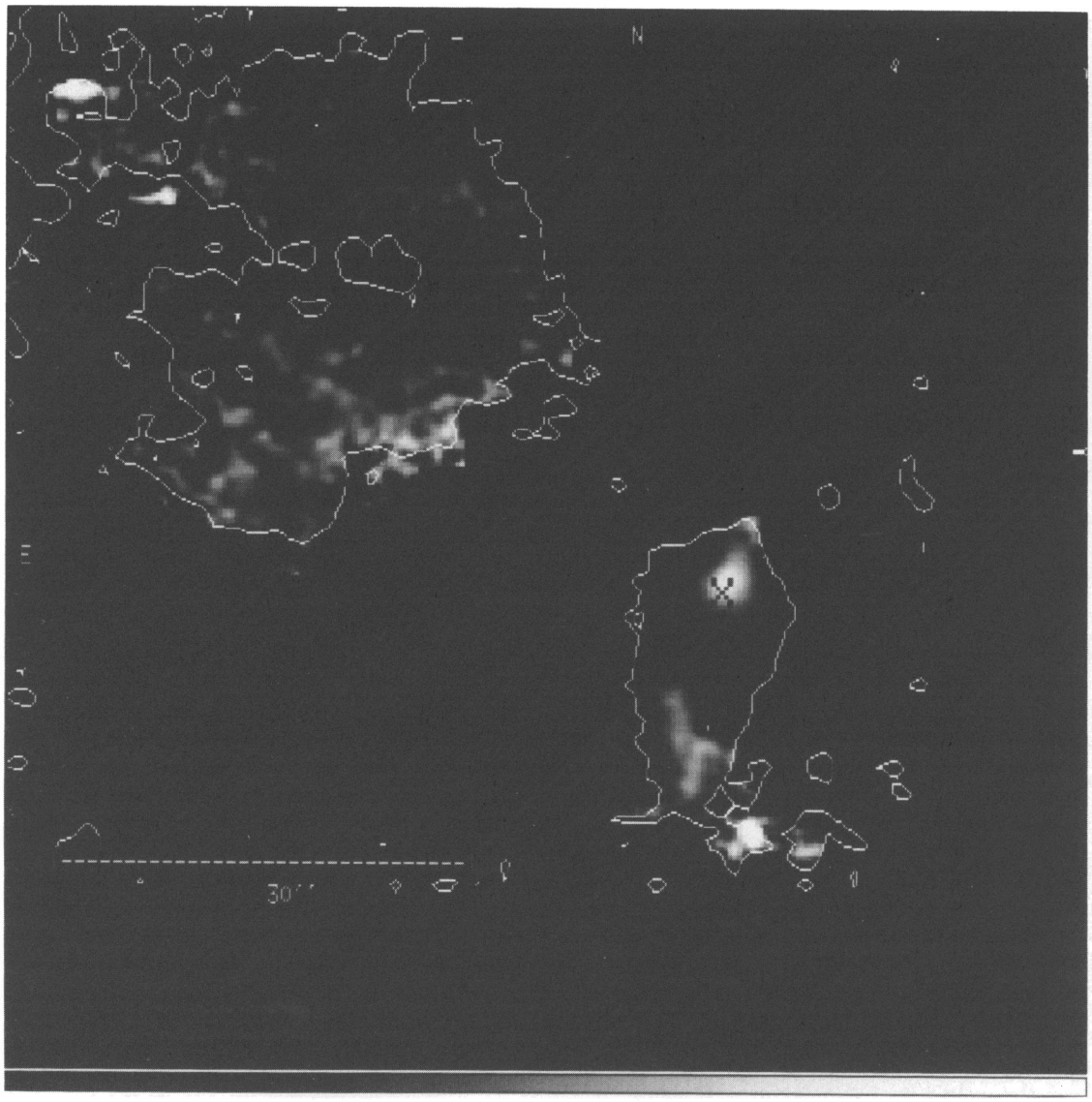

FIG. 12.—Dust extinction optical depth at 2.166 μm generated from a ratio of the Brα and the Brγ images. The image is scaled from 0 (*black*) to 4 (*white*) and is overlaid with 3 σ contours from the Brα image. The radio peak is marked with a cross.

thermal gas emission comprises $\sim$30% of the K-band emission in region K3-50A. Emission from heated dust grains, scattered light, and starlight all contribute to the remaining emission. Figure 13 shows the thermal gas emission at K, as estimated from the radio continuum emission in purple with the remaining emission sources in yellow. Both components have been been dereddened.

The (reddened) peak at H has shifted farther south, and the shape of the emission is elongated north-south. Thermal gas emission can account for $\sim$60% of the emission in region K3-50A. If the H image is first dereddened (see § 4.1), and then the contribution from thermal gas emission is subtracted off, the residual emission in the center of source K3-50A splits into three distinct peaks (see Fig. 14). The first is centered near the radio peak; the other two are centered near the peaks in extinction observed just north of the radio peak. Since we have already subtracted off the thermal gas component, we are seeing scattered light or thermal dust emission from three dense clumps, the first of which surrounds the ultracompact radio shell. Most of the remaining sources appear to be stars.

The (reddened) peak at J has shifted farther south, and we are only seeing that component of the scattered light that has a small amount of foreground extinction. It would be quite useful to measure the polarization of the NIR emission from this region to see how much of the emission is, in fact, scattered light.

Table 4 gives measurements of the broadband magnitudes of the likely ionizing stars of each H II region, the peak emission of K3-50A and K3-50C2, star 3 (to the west of K3-50A), and what appears to be star 5 (to the southeast of K3-50A) of Wynn-Williams et al. (1977) for comparison. Our broadband NIR measurements of K3-50A agree with those of Neugebauer & Garmire (1970) at H and K, and Neugebauer & Garmire's measurements at 3.5 and 4.8 μm are used to calibrate our L'' image.

4.3. *Regions K3-50A–D Supernova-induced Star Formation?*

Examining Figures 3 and 4, we see that extended emission is present from H II regions K3-50C1 and K3-50C2 to the northwest, through K3-50B and K3-50A, and connect-

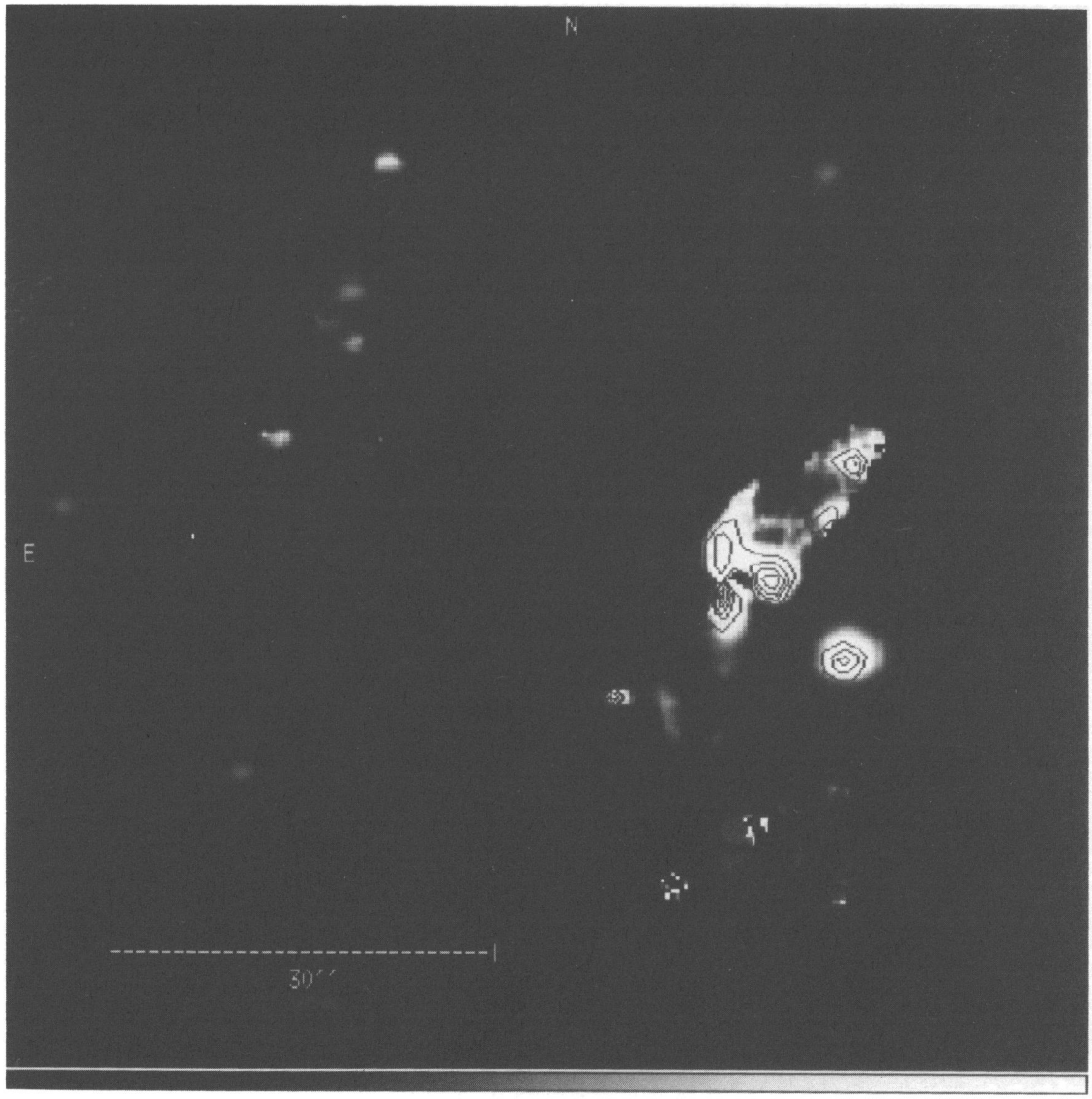

FIG. 14.—Dereddened image at H (1.65 μm) with the thermal gas component subtracted off

ing with K3-50D in the south. The whole structure forms an arc across the field extending some 5′.5. A bright source with extended emission is visible immediately north of the radio position of K3-50C2. A dust lane appears to extend across the south of K3-50C2 and completely obscures K3-50C1. There is a low-level extended emission to the south of this dust lane that appears to originate with K3-50C2. Nebulosity is also seen coincident with the very bright source located approximately halfway between K3-50B and K3-50C1.

The arc of emission formed by the H II regions may indicate that a shock wave from a recent supernova triggered star formation along the edge of a molecular cloud as material was swept up and compressed. If an ellipse is drawn along the outer edge of the H II regions, its origin lies $\sim 110''$ east of K3-50A. Its major axis is ~ 10 pc. If this scenario is correct, then the age of the supernova remnant (SNR) should be given, assuming spherical symmetry (Ward-Thompson 1991), by

$$R = \left(\frac{2E}{\rho_0}\right)^{1/5} t^{2/5} ,$$

where R is the radius of the shell (3×10^{19} cm), E is the energy of the supernova (assumed to be 10^{51} ergs; Chevalier 1977), ρ_0 is the preexplosion cloud density (3×10^{-21} g cm^{-3} for a typical giant molecular cloud [GMC]; Lang 1992), and t is the age of the SNR. This density gives an age of $\sim 2 \times 10^5$ yr. If instead we use the average density of the cloud as given by H I measurements (Bridle & Kesteven 1970) of 4 atoms cm^{-3}, we find an age of 9×10^3 yr. The lifetime of contraction to the main sequence of an O5 star is $\sim 6 \times 10^3$ yr (Clayton 1983). Each H II region K3-50A–D is thought to be excited by an O5 or higher mass star if there is a single ionizing source for each (Roelfsema et al. 1988). This contraction time gives a lower bound to the age of the SNR consistent with our previous result, since, if the supernova triggered this round of star formation, it had to occur before the protostars began their collapse. While these results do not definitively determine the existence of sequential star formation in this region, they are at least consistent, and the geometry is very suggestive. Examining the region near the location of the inferred supernova shows the existence of a dim, possible ringlike structure of clumps visible at H and K. We do not have any other information

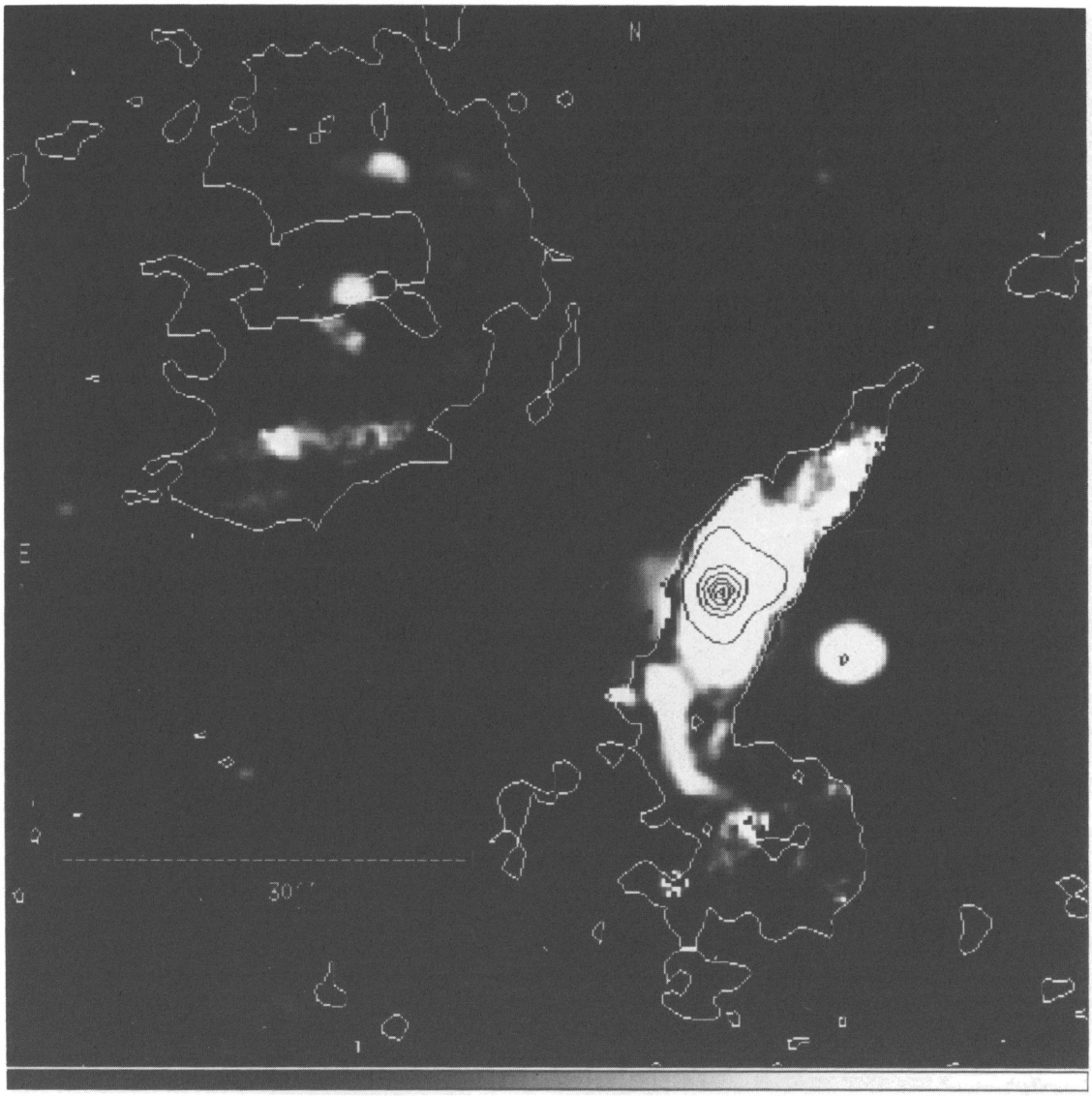

FIG. 15.—Dereddened image at K (2.23 μm). The outer contour is the 14.7 GHz 3 σ contour. Inside this contour the image has been corrected by an image of dust extinction optical depth. The inner contours trace the peak emission.

on this structure. No supernova remnant has been reported in a 3′ radius of this location in a literature search of the SIMBAD database.

5. THREE MICRON UNIDENTIFIED EMISSION FEATURE

5.1. *Emission Source*

Emission near 3.3 μm is generally attributed to the aromatic C—H stretch mode (Duley, Williams, & Moorhouse 1991). This mode arises in both hydrogenated graphitic carbon and PAH molecules/grains.

5.2. *Observations*

The 3.29 μm emission (teal) falls along and outside the outer edge of the H II region K3-50A, as traced out by the EOT 14.7 GHz radio continuum emission (red) along the southeastern extension of the H II region (Fig. 17 [Pl. 20]; see also Fig. 7). However, this emission is also coincident with the H II region along the brightest part of the radio continuum emission. We are probably seeing a thick shell of 3.29 μm emission surrounding and extending into the central H II region. In addition, ionizing radiation seems to be escaping the central H II region to the south, ionizing clumps of hydrogen and exciting 3.29 μm emission in surrounding small dust grains. Expected 3.29 μm emission surrounding the northern half of K3-50A is likely obscured by the same dust extinction seen in the optical depth maps (see Figs. 8 and 9).

The 3.29 μm emission in region K3-50B shows a double-shell structure that opens to the east with an extension beyond the H II region to the west, coming almost to a point. The entire structure looks like that of a bow shock, with an east-west relative velocity between the material emitting at 3.29 μm and the surrounding ISM. At first glance it appears that what we are seeing is a thick shell of material with 3.29 μm emission excited on both the outer and inner edges. It is unclear what could give rise to this sort of double-shell structure, if this is indeed the case. Alternatively, we may be just viewing column density enhancements that by chance give the appearance of a double-shell structure. Other objects such as AFGL 2591 (Forrest & Shure 1986) show multiple-shell structures in NIR broadband emission. These structures have been interpreted as arising from periodic episodes of mass loss associ-

PLATE 20

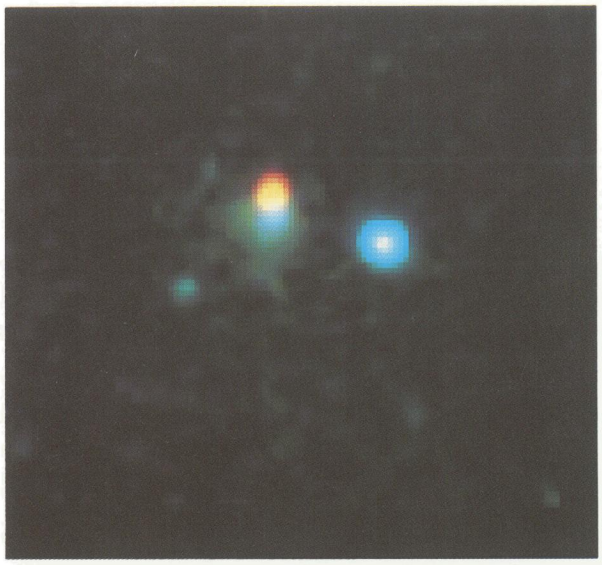

FIG. 2

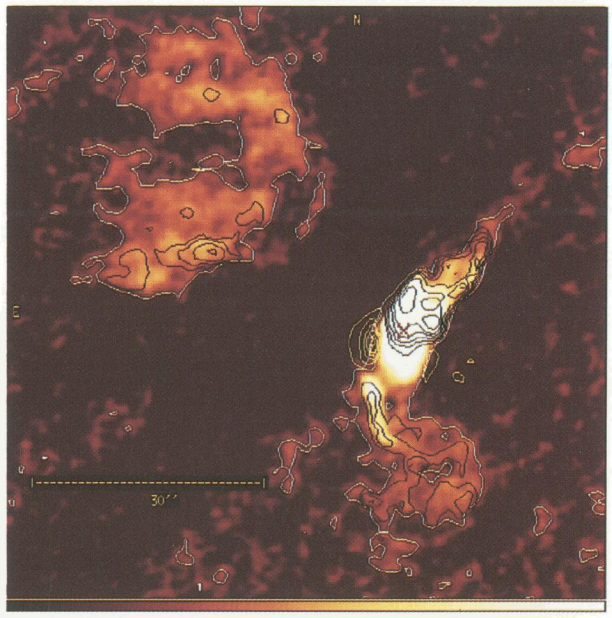

FIG. 8

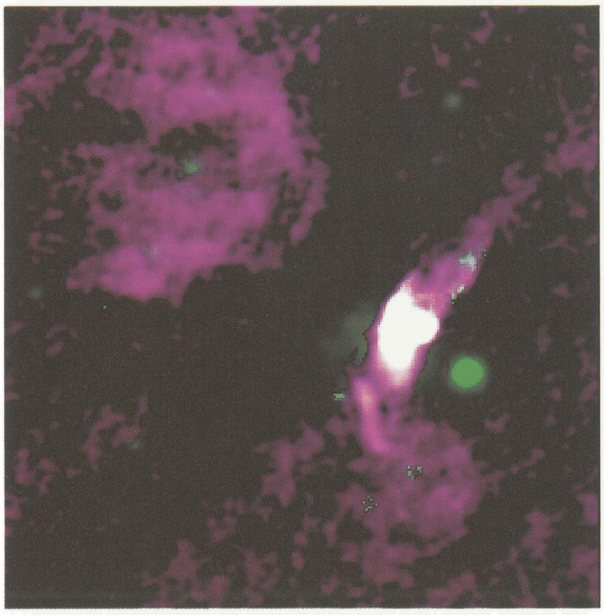

FIG. 13

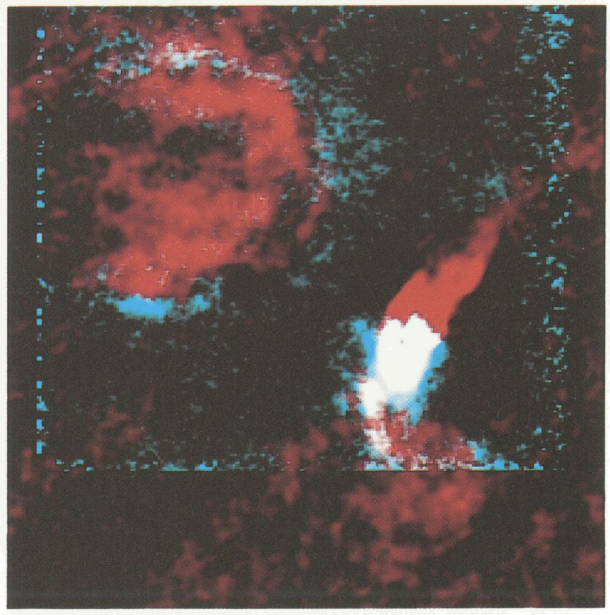

FIG. 17

FIG. 2.—"True color" image of K3 – 50A, J (1.23 μm), H (1.65 μm), and K (2.23 μm), are mapped to blue, green, and red, respectively. Object to the west is star 3 of Wynn-Williams (1977).

FIG. 8.—Equivalent optically thin 14.7 GHz radio continuum emission. White contours indicate 3 σ radio detection. Yellow contours trace regions of excess Brγ emission (i.e., scattered Brackett line emission; see § 3.1). Black contours trace dust extinction optical depth at 2.166 μm (see Fig. 9).

FIG. 13.—Composite, dereddened image at K (2.23 μm). The thermal gas component is displayed in purple; all other emission (scattered light, thermal dust emission, starlight) is displayed in green. Regions of overlap are indicated by white.

FIG. 17.—Emission at 3.29 μm (teal) overlaid on the radio continuum emission (red). Regions of overlap show as white.

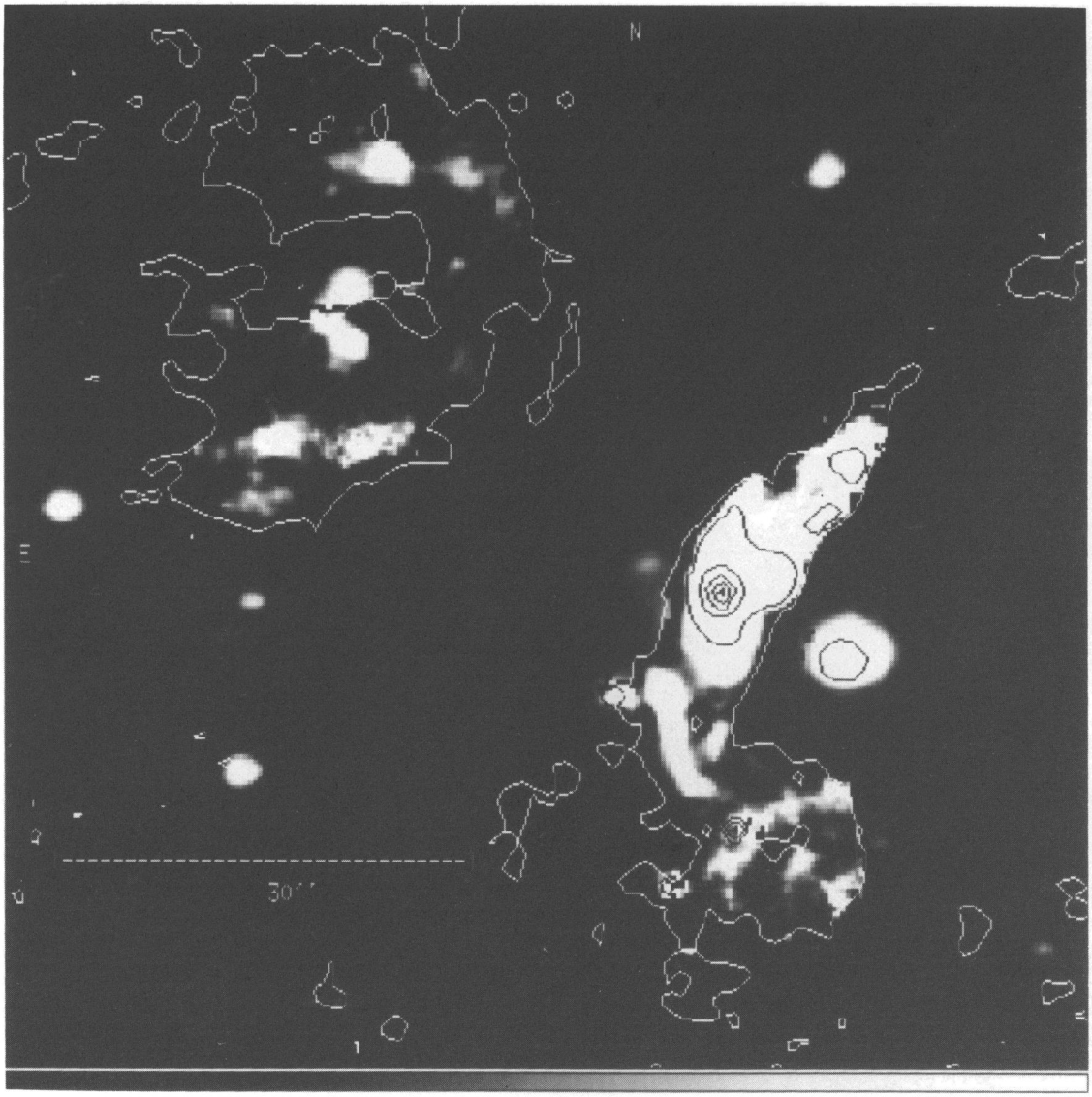

FIG. 16.—Dereddened image at H (1.65 μm). The outer contour is the 14.7 GHz 3 σ contour. Inside this contour the image has been corrected by an image of dust extinction optical depth. The inner contours trace the peak emission.

ated with star formation. The radio emission at 3.6 cm also shows a double-shell structure.

In general, the morphology of the 3.29 μm emission is quite similar to the emission at K, indicating that the very small dust grains emitting at 3.29 μm are found in the same region as the dust that is scattering light at 2.2 μm. This result is also found in the Mon R2 high-mass star formation region (Howard et al. 1994).

In NGC 7027, Woodward (1987) found that a significant fraction of the 3.29 μm emission present in this object must arise interior to the H II region, although $\geq 60\%$ of the feature emission arises from a thin shell just outside the ionized zone. This result indicates that, under at least some physical conditions, the material emitting at 3.29 μm is robust enough to survive a hard UV radiation field for a period of time; we are seeing a similar situation here in both regions K3-50A and K3-50B.

6. DISCUSSION

There is a high-velocity ^{12}CO outflow from K3-50A (Phillips & Mampaso 1991) that shows marginal evidence of bipolarity. There is a small separation (less than 9″) between the red and blue wing maxima along a northeast-to-southwest line, with the blue wing maxima being found southwest of the red wing. This CO map is the highest resolution ^{12}CO map available that shows the full velocity range. However, there is a positional error in this map. The map appears to be offset to the south by approximately 20″ from the true position (compare with ^{12}CO maps of Phillips et al. 1988; Sargent et al. 1985). Shifting the map $\sim$20″ north places the radio continuum peak, K3-50A, between the red and blue outflow peaks, and is consistent with the higher density tracer HCO^+ (Vogel & Welch 1983) and ^{13}CO (Sargent et al. 1985) maps falling in the center of the ^{12}CO cloud (see below).

The evidence of bipolarity is stronger in the outer, fainter CO contours, with the red wing extending to the east while the blue wing extends to the west. It has been postulated that this is a bipolar molecular outflow viewed nearly pole-on (Phillips & Mampaso 1991).

Sargent et al. (1985) also present interferometric ^{12}CO maps with 7″ resolution. While these maps do not cover the

TABLE 4

J (1.23 μm), H (1.65 μm), K (2.23 μm), AND L'' (3.81 μm) MAGNITUDES OF SOURCES IN $K3-50$ AS MEASURED IN 5″ SOFTWARE APERTURES

Source	Offsets from Star 3 at K (East, North) (arcsec)	J (mag)	H (mag)	K (mag)	L'' (mag)	Stellar Type[a]	A_V[a]
Star 3[b]	0.0, 0.0	9.90	9.49 (9.53)[c]	9.20 (9.26)[c]	8.28	Foreground	...
Star 5[d]	17.02, −2.98	13.07	12.50 (12.82)	11.41 (12.15)	...	B0[e]	5.8
A peak[f]	9.50, 4.86	11.66	10.62 (10.82)	7.91 (8.01)	3.39	<O6[g]	...
B star[h]	37.35, 27.75	...	11.91 (12.12)	10.92 (11.27)	...	O6	10.9
C1 star[i]	114.91, 92.91	...	15.25 (15.35)	14.64 (15.45)	...	A0	0.2
C2 star[j]	127.71, 95.76	...	15.86 (16.72)	14.44 (15.20)	...	B5	14.3
C2 peak[k]	128.22, 102.27	...	13.42 (13.91)	11.39 (11.89)	...	O6	19.5
D star 1[l]	35.92, −61.16	...	10.60 (10.69)	10.22 (10.41)	...	O6	3.1
D star 2[m]	25.78, −64.44	...	11.65 (11.85)	11.11 (11.49)	...	B0	1.3

[a] A least-squares fit to the H and K magnitudes of an O6, B0, B5, A0, F0, or G0 star at 8.7 kpc with varying degrees of extinction, using a $\lambda^{-1.8}$ extinction law in the near-infrared in combination with the Cardelli et al. 1989 result $A_v/A_k = 9.259$. Absolute visual magnitudes (V) were taken from Lang 1992, while infrared colors ($V-K$ and $H-K$) were taken from Koorneef 1983.

[b] Star 3 is identified with field star 3 from Wynn-Williams et al. 1977.

[c] Measurements in parentheses have the average nebular emission in an annulus around the object subtracted off. All other measurements are the total flux in a 5″ diameter circular aperture.

[d] Star 5 is identified with field star 5 from Wynn-Williams et al. 1977.

[e] High nebular contamination, possibly foreground.

[f] Measured at the peak of the infrared emission.

[g] Best fit indicates star is an earlier spectral type than an O6 star.

[h] Brightest star at K near the center of H II region B, possibly the exciting source. Note, however, that there are a number of pointlike sources within B.

[i] Faint star closest to the position of the radio peak.

[j] Faint star closest to the position of the radio peak.

[k] Measured at the peak of the infrared emission.

[l] Brightest star at the center of H II region D, probably the exciting source.

[m] Second bright star within H II region D.

full velocity range of the ^{12}CO emission, they show a structure that appears more disklike, lending support to the idea that the ^{12}CO traces the outer edges of the rotating core rather than originating in a bipolar outflow (see below).

The bipolar molecular outflow picture is inconsistent with the view of HCO^+ measurements presented by Vogel & Welch (1983). They imaged HCO^+ with a resolution of 11″.3 × 9″.5 and found a central dense core with a velocity gradient of 8 km s^{-1} pc^{-1} over a distance greater than 1 pc, consistent with a dense core rotating from west to east with its axis of symmetry in the plane of the sky. The velocity-integrated core is flattened north-south with an axial ratio of 2 to 1. It is difficult to understand how the molecular outflow from K3-50A could lie perpendicular to the line of sight when the symmetry axis of the rotating parent cloud is in the plane of the sky running approximately northwest to southeast, though there is the possibility that some other, low-mass star is the source of the extended CO outflow.

De Pree et al. (1994) find velocity gradients in the ionized gas from K3-50A consistent with a central east-west rotation and a bipolar ionized outflow to the northwest and to the southeast. They have proposed that the ionized gas outflow is directed by the presence of a flattened, circumstellar disk. The ionized bipolar outflow and the molecular bipolar outflow cannot be oriented perpendicular to each other if they originate from the same source. Furthermore, the ^{13}CO map shows a lobed structure indicative of a torus, viewed nearly equator-on. The lower emission between the two lobes lines up very well with the ionized outflow, indicating that the ionized flow lies in the "doughnut hole" of the dense gas torus. We suggest that the CO emission traces an outer extension of the rotating molecular cloud core seen in HCO^+ and ^{13}CO. The ^{12}CO emission covers a much higher velocity range (72.8 km s^{-1}; Phillips & Mampaso 1991) than the central core material (20.2 km s^{-1}; Vogel & Welch 1983).

The HCO^+ peak lies to the north of the continuum peak (region K3-50A). We are thus directly imaging parts of this dense core in our dust extinction optical depth maps (see Fig. 8). We find that the densest regions of dust cover the region north of K3-50A and extend west, at least to the southern part of region K3-50B. There is structure throughout the core, with $\lesssim 3''$ sized clumps in the regions of heaviest obscuration. The Brackett line emission from each of the clumps is consistent with emission from a high-mass (O or B-type) star (see § 3.5), though this emission could simply be extended emission from the central star at the radio peak.

Comparing our dust extinction optical depth map with high-resolution radio data of the central shell (Turner & Matthews 1984), we see that the morphology of the shell is consistent with a blister H II region that is, perhaps, breaking up. The morphology of the ring or shell may indicate that the ionizing star is offset from the center of the H II region toward the southeast, similar to the H II region surrounding Mon R2 (see Massi, Felli, & Simon 1985). However, the region of heaviest obscuration lies to the north. Combining this picture with the HCO^+ data indicates that a blister H II region formed in the southern central part of a core of dense rotating molecular material. The H II region formed in the cloud and then broke out toward less dense regions to the northwest, behind the cloud and to the south toward the front of the cloud, leaving a rotating torus of molecular material. Excess Brackett line emission, mentioned in § 3.1, appears to arise from scattering of Brackett line photons off the inner back

side of the "doughnut hole" formed by the bipolar ionized gas outflow breaking through the flattened cloud of dense gas. The southern arc of Brγ emission, as well as the 3.29 μm emission, trace out the edge of the cloud being ionized by emission escaping to the south of the central H II region, while the northern arc is predominantly obscured except at radio wavelengths. If the heavy dust obscuration were not present, similar emission to the north would be seen, as indicated in the radio maps and in the extinction-corrected IR images (Figs. 15 and 16).

7. SUMMARY

We have imaged the massive-star formation region K3-50 in a number of broadband, near-infrared wavelength bands, as well as at Brα, Brγ, and in the 3.29 μm unidentified emission band. Images of K3-50 in the Brackett emission lines compared with radio emission lead to an image of the small-scale line-of-sight extinction to the H II regions K3-50A and K3-50B.

The region is complicated; however, the many observations suggest a consistent three-dimensional view of region K3-50A, and perhaps the entire arc of star formation. A supernova shock wave, occurring 10^4–10^5 years ago, may have triggered this new round of star formation as it compressed material in the nearby molecular cloud giving rise to H II regions K3-50A, K3-50B, K3-50C1, K3-50C2, and K3-50D. One of the youngest objects in the region is the H II region K3-50A. A dense broken ring of ionized material surrounds the central object to the southeast, opening to the northwest. The ring appears to be inconsistent with limb brightening of a shell and may, thus, be broken along the line of sight as well. A dense torus of material, as traced out in HCO^+ and ^{13}CO, is rotating from west to east around this central source and is the birthplace of the high-mass star. The star and subsequent H II region formed in the center of this dense core, and ionized gas from the region broke through the dense molecular gas in a bipolar flow in front of the cloud extending to the south (blueshifted) and behind the cloud extending to the northwest (redshifted). ^{12}CO emission from the region appears to trace out the outer edges of the rotating cloud core rather than originating in a bipolar molecular outflow. The radio continuum emission of region K3-50A is consistent with excitation by a single O4 star; however, we do see some evidence, from clumping in the extinction map, that a cluster of stars may be forming rather that a single star. Vogel & Welch (1983) estimate the mass of the dense gas cloud surrounding region K3-50A as $\sim$2000 $M_\odot$, and they state that it is probably the precursor of an open cluster or association.

The H II regions K3-50B and K3-50D appear to be more evolved than K3-50A. Regions K3-50B and K3-50D have diameters between 1 and 1.5 pc and show classic shell structure. While region K3-50A falls under Churchwell's description of a "compact H II region" that is in the earliest phase of development of an H II region, regions K3-50B and K3-50D fall on the boundary between "compact H II region" and "expanding H II region." Region K3-50D is optically visible with only $\sim$2 mag of visual extinction (Roelfsema et al. 1988), while region K3-50B has an average A_V of $\sim$12 mag. The radio continuum of K3-50D is consistent with excitation by an O4 star, while that of K3-50B is consistent with excitation by an O4.5 star (Roelfsema et al. 1988).

Regions K3-50C1 and K3-50C2 are located behind $\sim$97 and 32 mag of visual extinction, respectively (Roelfsema et al. 1988), and both fall into the "compact H II region" category. K3-50C1 is completely obscured in our broadband H and K images, and falls in the center of a dust lane running east-west. The radio peak of K3-50C2 is obscured by the same dust lane; however, emission is observed to the immediate north of this object, indicating a region of lower obscuration to the north. Faint extended emission is also visible to the south of the radio peak. This indicates that we are probably observing a central obscuring disk or torus viewed nearly equator-on with the north side slightly facing the observer. A faint pont source is seen in the dust lane near the position of the radio source. K3-50C1 shows no clear emission at H or K. However, there is again a faint point source near the peak of the radio emission.

Following the complex of H II regions from south to north, there is a gradient in extinction, increasing to the north, that may indicate that the H II regions are embedded deeper in the molecular cloud in the northern regions of the complex than they are in the southern regions. However, the actual extinction gradients are not linear. There are large variations in the extinction associated with small-scale features that include local regions of high density to the immediate north of K3-50A, covering K3-50C1, and the central part of K3-50C2. The dense gas seems to be displaying the same filamentary nature on this scale as is seen on larger scales in H I (Read 1981).

The authors wish to thank those who helped in this project: S. Libonate, S. Solomon, and F. Piche for helping with the various observations; K. McFadden for computer support; B. Sklanka, C. McMurtry, and N. Shanmugalingam for transferring images; R. Gehrz for allocation of observing time and assistance at Mount Lemmon; C. Woodward for assistance at WIRO and B. Howell for allocation of time at WIRO; and D. Watson and A. Sargent for help finding the ^{13}CO maps of K3-50A. S. Solomon wrote the mosaicking software, and S. Libonate wrote the least-squares fitting routine used to determine the distortion and plate scale of the 58 × 62 images. The Astronomical Society of New York and the National Geographic Society provided funds for travel. The Third Generation Camera was built with a grant from the NSF. E. Howard was partially supported by a NASA Graduate Student Researchers Program grant. This research has made use of the SIMBAD database, operated at CDS, Strasbourg, France, as well as the NASA Astrophysical Data Service (ADS) Abstract Service.

REFERENCES

Bridle, A. H., & Kesteven, M. J. L. 1970, ApJ, 75, 902
Cardelli, J. A., Clayton, G. C., & Mathis, J. S. 1989, ApJ, 345, 245
Chevalier, R. A. 1977, ARA&A, 15, 175
Clayton, D. D. 1983, Principles of Stellar Evolution and Nucelosynthesis (Chicago: Univ. Chicago Press)
De Pree, C. G., Goss, W. M., Palmer, P., & Rubin, R. H. 1994, ApJ, 428, 670
De Pree, C. G., Mehringer, D. M., & Goss, W. M. 1996, in preparation
Draine, B. T., & Lee, H. M. 1984, ApJ, 285, 89
Duley, W. W., Williams, D. A., & Moorhouse, A. 1991, MNRAS, 253, 505

Forrest, W. J., & Shure, M. A. 1986, ApJ, 311, L81
Harris, S. 1975, MNRAS, 170, 139
Herter, T. 1981, Ph.D. thesis, Univ. Rochester
Herter, T., et al., 1981, ApJ, 250, 186
Howard, E. M., Pipher, J. L., & Forrest, W. J. 1994, ApJ, 425, 707
Koorneef, J. 1983, A&A, 128, 84
Lang, K. R. 1992, Astrophysical Data, Planets and Stars (New York: Springer), 144
Martin, P. G., & Whittet, D. C. B. 1990, ApJ, 357, 113
Massi, M., Felli, M., & Simon, M. 1985, A&A, 152, 387
Natta, A., & Panagia, N. 1984, ApJ, 287, 228
Neugebauer, G., & Garmire, G. 1970, ApJ, 161, L91
Panagia, N. 1973, AJ, 78, 929
Persson, S. E., & Frogel, J. A. 1974, ApJ, 188, 523
Phillips, J. P., et al. 1988, A&A, 190, 289
Phillips, J. P., & Mampaso, A. 1991, A&AS, 88, 189
Read, P. L. 1981, MNRAS, 195, 371
Roelfsema, P. R., Goss, W. M., & Geballe, T. R. 1988, A&A, 207, 132
Sargent, A. I., Scoville, N. Z., Masson, C. R., Claussen, M. J., Lo, K. Y., & Phillips, T. G. 1985, in Masers, Molecules and Mass Outflows in Star Forming Regions, ed. A. D. Haschi (Cambridge: Haystack Obs.), 215
Thompson, R. I., & Tokunaga, A. T. 1980, ApJ, 235, 889
Turner, B. E., & Matthews, H. E. 1984, ApJ, 277, 164
van de Hulst, H. C. 1946, Rech. Astron. Obs. Utrecht, 11, 1
Vogel, S. N., & Welch, W. J. 1983, ApJ, 269, 568
Ward-Thompson, D., & Robson, E. I. 1991, MNRAS, 248, 670
Woodward, C. 1987, Ph.D. thesis, Univ. Rochester
Woodward, C. E., Pipher, J. L., Shure, M., & Forrest, W. J. 1989, ApJ, 342, 860
Wynn-Williams, C. G., Becklin, E. E., Matthews, K., Neugebauer, G., & Werner, M. W. 1977, MNRAS, 179, 255